

# Searches for new physics below twice the electron mass with GERDA

The GERDA collaboration<sup>a</sup>,

M. Agostini<sup>10</sup>, A. Alexander<sup>10</sup>, G. Araujo<sup>21</sup>, A.M. Bakalyarov<sup>15</sup>,  
M. Balata<sup>1</sup>, I. Barabanov<sup>13,b</sup>, L. Baudis<sup>21</sup>, C. Bauer<sup>9</sup>, S. Belogurov<sup>14,13,c</sup>,  
A. Bettini<sup>18,19</sup>, L. Bezrukov<sup>13</sup>, V. Biancacci<sup>3</sup>, E. Bossio<sup>17</sup>, V. Bothe<sup>9</sup>,  
R. Brugnera<sup>18,19</sup>, A. Caldwell<sup>16</sup>, S. Calgari<sup>18,19</sup>, C. Cattadori<sup>11</sup>,  
A. Chernogorov<sup>14,15</sup>, P.-J. Chiu<sup>21</sup>, T. Comellato<sup>17</sup>, V. D'Andrea<sup>3</sup>,  
E.V. Demidova<sup>14</sup>, N. Di Marco<sup>2</sup>, E. Doroshkevich<sup>13</sup>, M. Fomina<sup>7</sup>,  
A. Gangapshev<sup>13,9</sup>, A. Garfagnini<sup>18,19</sup>, C. Gooch<sup>16</sup>, P. Grabmayr<sup>20</sup>,  
V. Gurentsov<sup>13</sup>, K. Gusev<sup>7,15,17</sup>, J. Hakenmüller<sup>9,d</sup>, S. Hemmer<sup>19</sup>,  
W. Hofmann<sup>9</sup>, J. Huang<sup>21</sup>, M. Hult<sup>8</sup>, L.V. Inzhechik<sup>13,e</sup>, J. Janicskó  
Csáthy<sup>17,f</sup>, J. Jochum<sup>20</sup>, M. Junker<sup>1</sup>, V. Kazalov<sup>13</sup>, Y. Kermaïdic<sup>9</sup>,  
H. Khushbakht<sup>20</sup>, T. Kihm<sup>9</sup>, K. Kilgus<sup>20</sup>, I.V. Kirpichnikov<sup>14</sup>,  
A. Klimenko<sup>9,7,g</sup>, K.T. Knöpfle<sup>9</sup>, O. Kochetov<sup>7</sup>, V.N. Kornoukhov<sup>13,c</sup>,  
P. Krause<sup>17</sup>, V.V. Kuzminov<sup>13</sup>, M. Laubenstein<sup>1</sup>, M. Lindner<sup>9</sup>, I. Lippi<sup>19</sup>,  
A. Lubashevskiy<sup>7</sup>, B. Lubsandorzhev<sup>13</sup>, G. Lutter<sup>8</sup>, C. Macolino<sup>3</sup>,  
B. Majorovits<sup>16</sup>, W. Maneschg<sup>9</sup>, G. Marshall<sup>10</sup>, M. Misiaszek<sup>5</sup>, M. Morella<sup>2</sup>,  
Y. Müller<sup>21</sup>, I. Nemchenok<sup>7,g</sup>, M. Neuberger<sup>17</sup>, L. Pandola<sup>4</sup>, K. Pelczar<sup>8</sup>,  
L. Pertoldi<sup>17,19</sup>, P. Piseri<sup>12</sup>, A. Pullia<sup>12</sup>, C. Ransom<sup>21</sup>, L. Rauscher<sup>20</sup>,  
M. Redchuk<sup>19</sup>, S. Riboldi<sup>12</sup>, N. Rumyantseva<sup>15,7</sup>, C. Sada<sup>18,19</sup>, S. Sailer<sup>9</sup>,  
F. Salamida<sup>3</sup>, S. Schönert<sup>17</sup>, J. Schreiner<sup>9</sup>, A-K. Schütz<sup>20,h</sup>, O. Schulz<sup>16</sup>,  
M. Schwarz<sup>17</sup>, B. Schwingenheuer<sup>9</sup>, O. Selivanenko<sup>13</sup>, E. Shevchik<sup>7</sup>,  
M. Shirchenko<sup>7</sup>, L. Shtembari<sup>16</sup>, H. Simgen<sup>9</sup>, A. Smolnikov<sup>9,7</sup>, D. Stukov<sup>15</sup>,  
S. Sullivan<sup>9</sup>, A.A. Vasenko<sup>14</sup>, A. Veresnikova<sup>13</sup>, C. Vignoli<sup>1</sup>, K. von  
Sturm<sup>18,19</sup>, T. Wester<sup>6</sup>, C. Wiesinger<sup>17</sup>, M. Wojcik<sup>5</sup>, E. Yanovich<sup>13</sup>,  
B. Zatschler<sup>6</sup>, I. Zhitnikov<sup>7</sup>, S.V. Zhukov<sup>15</sup>, D. Zinatulina<sup>7</sup>, A. Zschocke<sup>20</sup>,  
K. Zuber<sup>6</sup>, and G. Zuzel<sup>5</sup>.

<sup>1</sup> INFN Laboratori Nazionali del Gran Sasso, Assergi, Italy

<sup>2</sup> INFN Laboratori Nazionali del Gran Sasso and Gran Sasso Science Institute, Assergi, Italy

<sup>3</sup> INFN Laboratori Nazionali del Gran Sasso and Università degli Studi dell'Aquila, L'Aquila, Italy

<sup>4</sup> INFN Laboratori Nazionali del Sud, Catania, Italy

<sup>5</sup> Institute of Physics, Jagiellonian University, Cracow, Poland

<sup>6</sup> Institut für Kern- und Teilchenphysik, Technische Universität Dresden, Dresden, Germany

<sup>7</sup> Joint Institute for Nuclear Research, Dubna, Russia

<sup>8</sup> European Commission, JRC-Geel, Geel, Belgium

<sup>9</sup> Max-Planck-Institut für Kernphysik, Heidelberg, Germany

<sup>10</sup> Department of Physics and Astronomy, University College London, London, UK

<sup>11</sup> INFN Milano Bicocca, Milan, Italy

<sup>12</sup> Dipartimento di Fisica, Università degli Studi di Milano and INFN Milano, Milan, Italy

<sup>13</sup> Institute for Nuclear Research of the Russian Academy of Sciences, Moscow, Russia

<sup>14</sup> Institute for Theoretical and Experimental Physics, NRC "Kurchatov Institute", Moscow, Russia

<sup>15</sup> National Research Centre "Kurchatov Institute", Moscow, Russia

<sup>16</sup> Max-Planck-Institut für Physik, Munich, Germany

<sup>17</sup> Physik Department, Technische Universität München, Germany

<sup>18</sup> Dipartimento di Fisica e Astronomia, Università degli Studi di Padova, Padua, Italy

<sup>19</sup> INFN Padova, Padua, Italy

<sup>20</sup> Physikalisches Institut, Eberhard Karls Universität Tübingen, Tübingen, Germany

<sup>21</sup> Physik-Institut, Universität Zürich, Zurich, Switzerland

**Abstract** A search for full energy depositions from bosonic keV-scale dark matter candidates of masses between 65 keV and 1021 keV has been performed with data collected during Phase II of the GERmanium Detector Array (GERDA) experiment. Our analysis includes direct dark matter absorption as well as dark Compton scattering. With a total exposure of 105.5 kg yr, no evidence for a signal above the background has been observed. The resulting exclusion limits deduced with either Bayesian or Frequentist statistics are the most stringent direct constraints in the major part of the 140-1021 keV mass range. As an example, at a mass of 150 keV the dimensionless coupling of dark photons and axion-like particles to electrons has been constrained to  $\alpha'/\alpha < 8.7 \times 10^{-24}$  and  $g_{ae} < 3.3 \times 10^{-12}$  at 90% credible interval (CI), respectively.

Additionally, a search for peak-like signals from beyond the Standard Model decays of nucleons and electrons is performed. We find for the inclusive decay of a single neutron in  $^{76}\text{Ge}$  a lower lifetime limit of  $\tau_n > 1.5 \times 10^{24}$  yr and for a proton  $\tau_p > 1.3 \times 10^{24}$  yr at 90% CI. For the electron decay  $e^- \rightarrow \nu_e \gamma$  a lower limit of  $\tau_e > 5.4 \times 10^{25}$  yr at 90% CI has been determined.

## 1 Introduction

The main goal of the GERDA experiment was to search for the neutrinoless double-beta ( $0\nu\beta\beta$ ) decay of  $^{76}\text{Ge}$ . An array of high-purity germanium (HPGe) detectors enriched up to  $\sim 87\%$  in  $^{76}\text{Ge}$  was employed in an active liquid argon (LAr) shield. The shielded environment and the excellent energy resolution of the Ge detectors made the experiment also suitable for the search of peak-like signatures induced by new physics processes other than  $0\nu\beta\beta$  decay. In this paper, searches for keV-scale bosonic dark matter (DM) interactions and single-particle disappearance processes are reported.

GERDA is sensitive to pseudoscalar (axion-like particles, ALPs) and vector (dark photons, DPs) bosonic DM candidates, sometimes referred to as super Weakly Interacting Massive Particles (superWIMPs) [1]. A previous search for photoelectric-like absorption of bosonic DM candidates, with masses<sup>1</sup> up to 1 MeV, was reported by GERDA in [2]. In this paper, a second interac-

tion process, i.e. the dark Compton scattering process, was included in the calculation of the interaction rate of these DM particles with electrons [3, 4]. Despite its lower detection efficiency at higher masses (see Table 2), the dark Compton scattering benefits from a larger interaction cross-section for energies above  $\sim 140$  keV [3].

Moreover, the experiment can probe beyond the Standard Model (BSM) decay processes violating conservation laws of the Standard Model (SM), e.g., the decay of a single neutron or proton [5]. As pointed out by Sakharov, the violation of the conservation of baryon number is one of the three fundamental criteria needed to be fulfilled to produce the matter-antimatter asymmetry in the early Universe [6]. GERDA explores the disappearance of a single nucleon in  $^{76}\text{Ge}$  by looking for the  $\beta$ -decay of the  $^{75}\text{Ge}$  ground state to an excited state of  $^{75}\text{As}$  in coincidence with the  $\gamma$ -ray emitted in the subsequent  $^{75}\text{As}$  de-excitation. The population of the  $^{75}\text{Ge}$  ground state follows the disappearance of either a neutron or a proton in  $^{76}\text{Ge}$ . Proton decay, in particular, populates first the unstable  $^{75}\text{Ga}$  nucleus that later decays by  $\beta$ -emission to  $^{75}\text{Ge}$ .

Another BSM process of interest is the decay of an electron via  $e^- \rightarrow \nu_e \nu_e \nu_e$  or  $e^- \rightarrow \nu_e \gamma$ , where the latter channel is explored in this study. It allows a sensitive test of the U(1) gauge symmetry that ensures the stability of the electron as well as the zero mass of the photon.

The paper is structured as follows. In Sect. 2, the theoretical framework for the bosonic DM and single-particle disappearance searches are introduced. In Sect. 3 an overview of the GERDA setup is given, focusing on the data selection and the evaluation of detection efficiencies for the final states of interest. In Sect. 4, Frequentist and Bayesian analysis methods, are sketched that are used in our data analysis. In Sect. 5, results obtained with both statistical frameworks are presented. Conclusions are drawn in Sect. 6.

## 2 Approaches to the search for new physics

### 2.1 Bosonic dark matter

Several galactic and cosmological observations indicate the existence of DM. However, its nature is still unknown. In the cosmological standard model  $\Lambda\text{CDM}$  the energy density contains 27% of DM, with the rest being ordinary matter (5%) and dark energy (68%). Hence, several laboratory studies have been conducted or are planned to detect and investigate the nature of DM [7]. Various theoretical models for DM candidates have been proposed for masses ranging over many orders of magnitudes [8]. In the energy range explored by GERDA,

<sup>a</sup> *correspondence:* gerda-eb@mpi-hd.mpg.de

<sup>b</sup> *deceased*

<sup>c</sup> *also at:* NRNU MEPhI, Moscow, Russia

<sup>d</sup> *present address:* Duke University, Durham, NC USA

<sup>e</sup> *also at:* Moscow Inst. of Physics and Technology, Russia

<sup>f</sup> *present address:* Semilab Zrt, Budapest, Hungary

<sup>g</sup> *also at:* Dubna State University, Dubna, Russia

<sup>h</sup> *present address:* Nuclear Science Division, Berkeley, USA

<sup>1</sup>In this paper, natural units are used, i.e.  $c = 1$ .

bosonic keV-scale DM particles are particularly interesting candidates. Masses within this range imply a super-weak interaction strength between the DM and the SM sector, much weaker than normal weak-scale interactions. The mass and the cross-section requirements follow directly from the necessity of having an early thermal decoupling of the DM sector, which happened before the electroweak epoch at  $T_{EW} \sim 100$  GeV [1]. In this paper, pseudoscalar and vector bosonic DM candidates are considered, focusing on masses below  $2m_e \sim 1022$  keV, where  $m_e$  is the electron mass. For DM masses  $m_{DM} \geq 2m_e$ , decays into  $e^-e^+$  pairs are possible, making long-lived DM highly unlikely. Below this threshold, bosonic DM candidates are stable at the tree level. In addition, radiative decays of ALPs and DPs into photons are possible at loop level in the keV-MeV range [1, 9].

The previous GERDA study focused on the bosonic DM absorption in processes analogous to the photoelectric effect. Here, the DM particle is completely absorbed by a detector's atom, which later releases an electron in the final state. The expected signal is a full absorption peak at the rest mass of the DM, assuming these DM particles have very small kinetic energies at  $\beta = v_{DM} \sim 10^{-3}$ . The peak is then broadened due to the detector's energy resolution. The photoelectric-like absorption cross section at a given mass is [1]

$$\sigma_{a,e}(m_a) = g_{ae}^2 \frac{m_a^2 \sigma_{pe}(m_a)}{\beta} \left( \frac{3}{16\pi\alpha m_e^2} \right) \quad (1)$$

and

$$\sigma_{V,e}(m_V) = \frac{\alpha'}{\alpha} \frac{\sigma_{pe}(m_V)}{\beta} \quad (2)$$

for pseudoscalar and vector DM candidates, respectively. Here,  $m_a$  ( $m_V$ ) is the ALP (DP) mass and  $\sigma_{pe}$  is the energy-dependent photoelectric cross-section of Ge. Assuming a DM density of  $\rho_{DM} = 0.3$  GeV cm $^{-3}$  and a corresponding average DM flux  $\Phi_{DM}$  per barn (b) and day (d) at Earth [10],

$$\Phi_{DM}(m_{DM}) = \beta \frac{7.8 \times 10^{-4}}{m_{DM}/[\text{keV}]} \text{b}^{-1} \text{d}^{-1}, \quad (3)$$

above cross sections are converted to the absorption interaction rate for pseudoscalar and vector DM, respectively, [2]

$$R_a^A = \frac{1.47 \times 10^{19}}{M_{tot}} g_{ae}^2 \left( \frac{m_a}{[\text{keV}]} \right) \left( \frac{\sigma_{pe}}{[\text{b}]} \right) \text{kg}^{-1} \text{d}^{-1} \quad (4)$$

and

$$R_V^A = \frac{4.68 \times 10^{23}}{M_{tot}} \frac{\alpha'}{\alpha} \left( \frac{[\text{keV}]}{m_V} \right) \left( \frac{\sigma_{pe}}{[\text{b}]} \right) \text{kg}^{-1} \text{d}^{-1} \quad (5)$$

where  $M_{tot}$  (g/mol) is the molar mass of the target material. The ALPs and DPs dimensionless couplings to electrons are parametrized via  $g_{ae}$  and  $\alpha'/\alpha$ , respectively. In particular,  $\alpha'$  denotes the hidden sector fine structure constant and is related to the kinetic mixing strength  $\kappa$  of DPs via  $\alpha' = \alpha\kappa^2$  [11]. For absorption of DPs, the expression in Eq. (5) is only valid for  $m_V \gtrsim 100$  eV where in-medium effects are negligible [11, 12]. Compared to the former GERDA publication, the rate constants of proportionality were recalculated. A more precise numerical value of 1.47 instead of 1.2 and 4.68 instead of 4 was obtained for ALPs and DPs, respectively. These estimates align with the numbers published in [13].

In this study, a second process has been included. This is the dark Compton scattering  $DM + e^- \rightarrow e^- + \gamma$  causing the release of a photon and an electron with fixed energies. For a non-relativistic incident DM particle having an energy equal to  $\omega \approx m_{DM}$ , the recoil energy  $T$  of the electron and the energy  $\omega'$  of the emitted photon are [4]

$$T = \frac{\omega^2}{2(m_e + \omega)} \quad \text{and} \quad \omega' = \sqrt{T^2 + 2m_e T}. \quad (6)$$

Adapting rate formulas from [4], the dark Compton interaction rate becomes

$$R_a^C = f_a^C N_e \frac{1.27 \times 10^{24}}{M_{tot}} g_{ae}^2 \left( \frac{[\text{keV}]}{m_a} \right) \text{kg}^{-1} \text{d}^{-1} \quad (7)$$

and

$$R_V^C = f_V^C N_e \frac{7.79 \times 10^{22}}{M_{tot}} \frac{\alpha'}{\alpha} \left( \frac{[\text{keV}]}{m_V} \right) \text{kg}^{-1} \text{d}^{-1}, \quad (8)$$

where  $N_e$  is the number of electrons of the target atom. The mass-dependent factors for ALPs and DPs are, respectively,

$$f_a^C(m_a) = \frac{m_a^2 (m_a + 2m_e)^2}{(m_a + m_e)^4} \quad (9)$$

and

$$f_V^C(m_V) = \frac{(m_V + 2m_e) (m_V^2 + 2m_e m_V + 2m_e^2)}{(m_V + m_e)^3}. \quad (10)$$

As shown in [3] higher total interaction rates are expected for DM particle masses above  $\sim 100$  keV when including the dark Compton scattering process. In a realistic experimental environment, different scenarios are possible depending on the efficiency with which the final state particles are detected. The focus here is on events in which both the final electron and photon are detected within a single Ge detector, leading to a signal at energy  $T + \omega' = m_{DM}$ . The spectral shape of the

signal in this absorption plus dark Compton scattering search is the same as in a pure absorption search, with the difference that the total expected signal is given by the sum of both contributions.

## 2.2 Nucleon decay

Baryon and/or lepton number conservation violating single- and multi-nucleon decays are predicted in several extensions of the SM. High nucleon decay lifetime sensitivities were already reached for light nuclei by tonne-scale experiments (see selected constraints listed in Sect. 5.2). In this work, the inclusive, i.e. mode-independent, decay of a single neutron and proton in  $^{76}\text{Ge}$  is investigated. In the former, a neutron would disappear in a  $^{76}\text{Ge}$  nucleus, leading to an excited  $^{75}\text{Ge}$  nucleus if no particles other than photons are emitted. The energy release of approximately 9.4 MeV corresponds to the lowest nuclear separation energy for a nucleon in  $^{76}\text{Ge}$  [14, 15], which could then be observed. As in this energy release, neither the number of photons emitted nor their angular distribution is unique, the energy deposition in the GERDA detector array following such decay is difficult to model. Hence, the subsequent low energy  $\beta$ -decay of the ground state  $^{75}\text{Ge}$  to an excited state of  $^{75}\text{As}$ , followed by a  $\gamma$  de-excitation of the daughter nucleus, is considered. The dominant decay channel searched for in this analysis is the  $\beta$ -decay to the 264.60 keV level ( $E_\beta = 912.6$  keV, 11.5% branching ratio), which is followed by the emission of a 264.60 keV photon (see Fig. 1).

The same method applies to the disappearance of a single proton. If a proton decays without the emission of accompanied nucleons, the produced  $^{75}\text{Ga}$  isotope undergoes  $\beta$ -decay to  $^{75}\text{Ge}$  with a half-life of 126(2) s and a branching ratio of 100% [16]. Given that both neutron and proton decays can be probed with the coincident  $^{75}\text{As}$  264.60 keV photon, this search is referred to as nucleon decay in the rest of the article.

This study aims to establish limits for nucleon disappearance in  $^{76}\text{Ge}$  which has, to our knowledge, not yet been probed.

## 2.3 Electron decay

Many laboratory tests have been performed to test the fundamental U(1) gauge symmetry ensuring charge conservation (see selected constraints listed together with our results in Sect. 5, Table 5). The decay of an electron violating charge conservation could happen through the emission of three neutrinos,  $e^- \rightarrow 3\nu_e$ , or a neutrino and a  $\gamma$ -ray,  $e^- \rightarrow \nu_e\gamma$ . The former process has a maximal

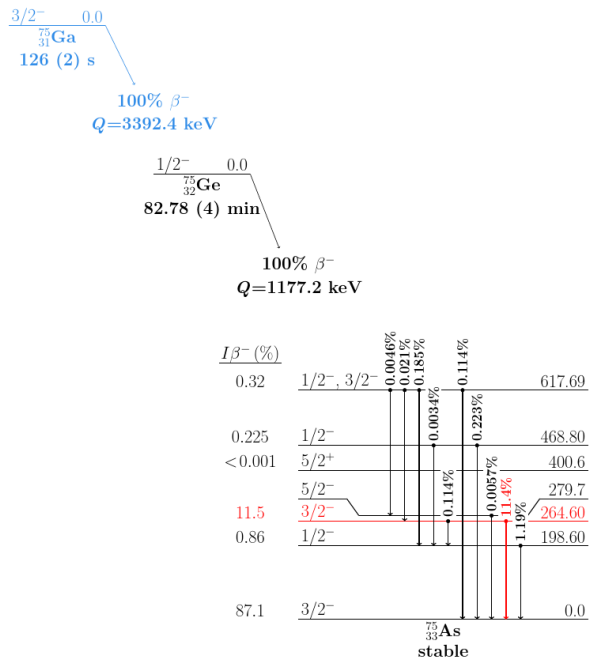


**Fig. 1** Scheme of the  $^{75}\text{Ge}$  ground state  $\beta$ -decay to  $^{75}\text{As}$  and subsequent  $\gamma$ -decays, adapted from [16]. The  $\beta$ -decay ( $E_\beta = 912.6$  keV) to the second excited  $^{75}\text{As}$  state in coincidence with the 264.60 keV  $\gamma$ -ray is used to tag both the neutron and proton disappearance in  $^{76}\text{Ge}$ . Level and  $\gamma$ -ray of interest are highlighted in red. The transition  $^{75}\text{Ge} \rightarrow ^{75}\text{As}$  following  $^{76}\text{Ge}$  proton decays is shown in blue

energy deposition that is equal to the maximal electron binding energy of  $^{76}\text{Ge}$  of  $\sim 11.1$  keV [17]. As this value is below the trigger threshold of GERDA, this signature could not be used in this study. Instead, the decay  $e^- \rightarrow \nu_e\gamma$  was analysed. The peak is expected to lie around half of the electron mass, i.e. at  $E_\gamma \sim 255.5$  keV. In addition, the release of the relevant atomic binding energies causes both a Doppler broadening and a shift of the 255.5 keV peak for different electron atomic levels. In our setup electron decays could occur both within a germanium detector as well as in its surrounding materials which include neighbored germanium detectors and LAr. If an electron decays within a detector's sensitive volume, both the photon energy and the one coming from the rearrangement of atomic shells, i.e. from X-rays or Auger electrons, are detected. Hence, for the  $i$ -th atomic shell with binding energy  $E_{b,i}$ , the total energy is

$$E_{t,i} = \frac{m_e - E_{b,i}}{2} + E_{b,i} = \frac{m_e + E_{b,i}}{2}. \quad (11)$$

In the case of an electron decaying outside the recording detector, the total detected energy equals

$$E_{t,i} = \frac{m_e - E_{b,i}}{2}. \quad (12)$$

Using Eq. (11) and the information provided in Sect. A of the Appendix the total energy recorded in a given germanium detector is expected to lie at 256.0 keV for electrons decaying within the detector’s sensitive volume. Additionally, GERDA germanium detectors can detect outgoing photons coming from neighbouring germanium material undergoing the electron decay as well as from the surrounding LAr. Hence, using Eq. (12), outgoing photons with energies of 255.0 keV and 255.3 keV, respectively, can be tagged. For each of these three contributions, the signal energy was derived as a weighted mean of energies  $E_{t,i}$  with the electron occupancy numbers as weights. Germanium and argon binding energies used in Eqs. (11) and (12) are listed in the Appendix (see Table 6 in Sect. A). The total signal energy is expected to be 255.9 keV by weighting for different source masses, electron occupancy numbers and detection efficiencies (see Eq. (A.3) in Sect. A). Other surrounding materials, e.g. detector holders or electronic components, were not taken into account. Because of their low mass, they do not alter the results by more than a few percent. The corresponding Doppler broadened line shape was determined as described in [18]. A discussion of the signal shape used in the present analysis is provided in the Appendix (see Sect. A). Figure 2 shows the final line shape, obtained by convolving the Doppler profile with a weighted Gaussian mixture distribution modelling the expected resolution broadening caused by the finite detector resolution (see Sect. 4.1). For the mixture model, the weights are defined as the exposures of each data set, separated by detector type and data-taking phase (see Sect. 3). Considering the contributions of source detectors, surrounding detectors, and the LAr, the convolution yields a full width at half maximum (FWHM) of 5.2 keV, where the mixture model contributes 2.0 keV, and the full Doppler-broadened line 4.4 keV.

### 3 Details of the GERDA experiment

The GERDA experiment was located underground at the Laboratori Nazionali del Gran Sasso (LNGS) of INFN, in Italy, under the Gran Sasso mountain. The rock overburden offers a shield of about 3500 m water equivalent, reducing the cosmic muon flux by six orders of magnitude [19]. Started in December 2015, the second phase of the experiment used 10 coaxial (Coax) detectors, 3 of them having a natural  $^{76}\text{Ge}$  isotopic abundance, together with 30 enriched Broad Energy Germanium (BEGe) detectors [20]. In October 2017, the energy trigger threshold of detectors was lowered from  $\mathcal{O}(100)$  to  $\mathcal{O}(10)$  keV. Data taking was interrupted in April 2018 for a hardware upgrade by replacing one

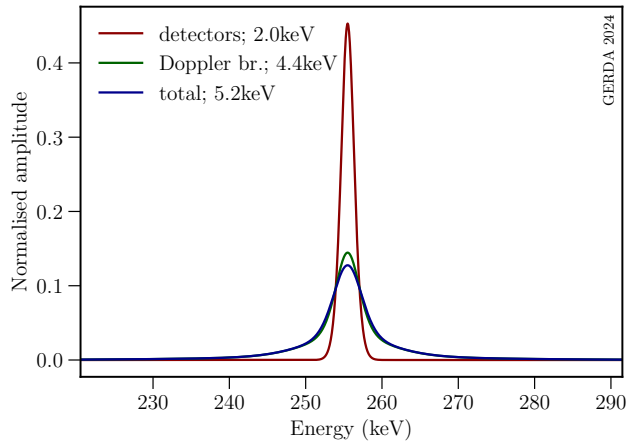


**Fig. 2** The contributions from detector resolution (red) and the Doppler-broadening (green) of lines from electron decay in the different atomic shells of germanium and argon (see Sect. 4.1). The total expected line shape of the electron decay signal at 255.9 keV is shown in blue. All Gaussians are normalized to unit area. Indicated resolution values are given in FWHM

enriched Coax detector ( $\sim 1$  kg) and all natural Coax detectors by 5 new enriched inverted coaxial (IC) detectors, with a total mass of 9.6 kg [21]. Data taking was resumed in July 2018 and lasted until November 2019. Here, data collected before (after) the 2018 upgrade are referred as Phase II (Phase II+) data. HPGe detectors were arranged in 7 strings, each of them enclosed in a transparent nylon cylinder that mitigates the  $^{42}\text{K}$  background [22]. The 7-string array was operated inside a 64 m<sup>3</sup> LAr cryostat [23] which provided both cooling and a high purity, active shield against background radiation. To detect scintillation light, the LAr volume around the array was instrumented with a curtain of wavelength-shifting fibers coupled to silicon photo-multipliers. Additionally, 16 cryogenic photomultiplier tubes (PMTs) were mounted on the copper plates at the two ends of the cylindrical LAr volume [20, 24]. During the 2018 upgrade, the geometrical fiber coverage was improved with the addition of an inner curtain [21]. The LAr cryostat was placed inside a tank containing 590 m<sup>3</sup> of ultra-pure water. The water tank was instrumented with 66 PMTs that help to detect Cherenkov light coming from muons passing through the experimental volume. The muon-induced background was further reduced to negligible levels by operating plastic scintillator panels placed on the roof of the clean room [25].

### 3.1 Data selection

In this paper, only Phase II and II+ data collected after the installation of the LAr veto system [20] were considered. Different data sets were used for bosonic DM and particle disappearance searches. Table 1 shows the exposure levels evaluated for enriched Coax, BEGe and IC detectors, during different periods of data taking. Natural coaxial detectors were left out of the analysis because of their unstable behaviour that translated into low duty factors. Pulse shape discrimination (PSD) cuts, which had been optimised for the  $0\nu\beta\beta$  decay search, were not applied in this study. Total exposure for all searches is 105.5 kg yr except for the bosonic DM search below 196 keV where it is 60 kg yr (see below).

**Table 1** Exposures accumulated with indicated detector types during GERDA Phase II (up to April 2018) and Phase II+ (from July 2018).  $R$  denotes the energy range of the respective spectra used for analysis in the bosonic DM search. At the chosen energy bin size of 1 keV (see Sect. 4.1) exposures for the energy intervals of 65 – 195 keV and 196 – 1021 keV are  $\mathcal{E}_1=60.0$  kg yr and  $\mathcal{E}_2=105.5$  kg yr, respectively.

Data collection	$R$ (keV)	Exposure (kg yr)		
		Coax	BEGe	IC
Dec 2015 - Oct 2017	196-1021	21.1	24.4	-
Oct 2017 - Apr 2018	65-1021	7.5	8.4	-
Jul 2018 - Nov 2019	65-1021	13.2	22.2	8.7

All searches share the same set of cuts, except the search for nucleon decay where the simultaneous firing of two detectors is required. This cut is henceforth referred to as the multiplicity 2 (M2) cut. Quality cuts were applied to remove non-physical events starting from the inspection of waveform parameters. Additionally, muon-induced events and events leading to energy depositions in the LAr were vetoed.

*Bosonic dark matter* A generic peak search was performed to look for signatures of a monoenergetic peak caused by the interaction of bosonic DM. The energy spectrum was filled only with events of multiplicity one (M1), i.e. events triggering only one Ge detector. A histogram of the final M1 data set is shown in Fig. 3. The bosonic DM analysis is performed in the interval 65(196)-1021 keV. The upper interval edge was fixed below  $2m_e$ , the energy threshold of decays into electron-positron pairs. The lower energy bound was motivated by the analysis threshold of the Ge detector. Until October 2017, events were accepted if their energy exceeded  $\geq 195$  keV. Afterwards, the detector

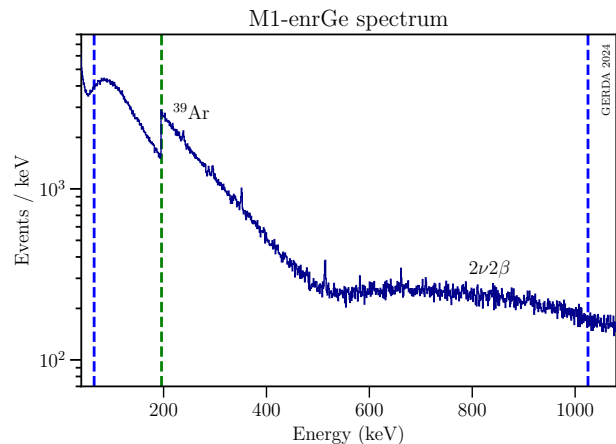


**Fig. 3** Combined GERDA Phase II/II+ spectrum of event multiplicity 1 after quality, muon veto, and LAr cuts. The dominant background contributions from  $^{39}\text{Ar}$   $\beta$  decay and  $^{76}\text{Ge}$   $2\nu\beta\beta$  decay are indicated. The green dashed line separates the regions 65 – 195 keV and 196 – 1021 keV with exposure  $\mathcal{E}_1 = 60.0$  kg yr and  $\mathcal{E}_2 = 105.5$  kg yr, respectively (see Table 1). The blue dashed lines mark the energy range inspected for bosonic DM candidates, i.e. 65-1021 keV

thresholds were lowered, thus, in addition, the data starting from 65 keV became available for this analysis. This change of thresholds causes the jump around 195 keV in the M1 energy spectrum of Fig. 3. More details are given in the Appendix (see Sect. B). The  $^{39}\text{Ar}$   $\beta^-$  decay is well visible, up to the end-point energy of 565(5) keV [26]. This  $^{39}\text{Ar}$  background is the reason why only full energy depositions were considered also for the dark Compton scattering process. Beyond  $\sim 500$  keV, the background continuum is dominated by the  $^{76}\text{Ge}$  two-neutrino double-beta ( $2\nu\beta\beta$ ) decay characterized by an end-point energy of  $Q_{\beta\beta} = 2039.06$  keV [21]. After applying the LAr cut, an almost clean  $2\nu\beta\beta$  decay spectrum is observed (see Sect. 4.2).

*Nucleon decay* The study of a single nucleon decay in  $^{76}\text{Ge}$  was performed by searching for a  $\beta$  particle with maximum energy  $E_\beta = 912.6$  keV and a coincident  $\gamma$ -ray of energy  $E_\gamma = 264.60$  keV (see Fig. 1). The emitted  $\beta$  particle is expected to be seen in the same detector where the nucleon decay happened since the range of an electron in germanium material is of  $\mathcal{O}(10\mu\text{m} - 1\text{mm})$  for the energy range from 50 keV to 1 MeV [27]. The photon may escape and propagate through the LAr to a neighbouring detector. Although the probability of this scenario is rather low, using this coincident tagging in two HPGe detectors strongly reduces the background. In a M2 event with energies  $(E_1, E_2)$  and  $E_1 + E_2 < Q_\beta + 2 \cdot \text{FWHM}(Q_\beta)$ , the partner with energy  $E_{1(2)}$  is classified as  $\gamma$  candidate if: i)  $E_{2(1)} <$

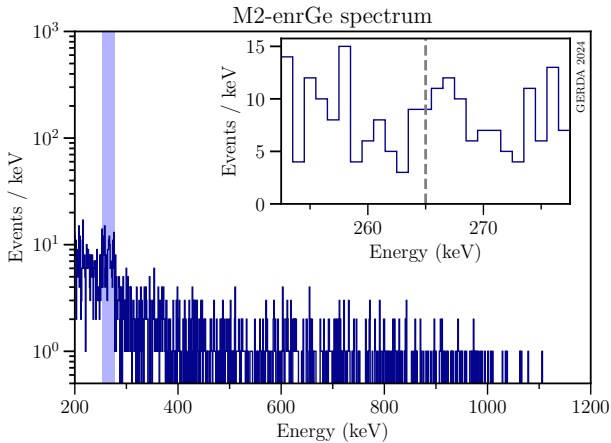


**Fig. 4** Histogram of multiplicity 2 (M2) events; see text for more details. The spectrum accounts for M2 events that survived quality cuts as well as muon and LAr vetoes. The inset shows the data in the  $\gamma$ -window (blue band) inspected for the nucleon decay signal, i.e.  $E_\gamma \pm 12.5$  keV with  $E_\gamma \sim 265.0$  keV (gray dashed line)

$E_\beta + 2 \cdot \text{FWHM}(E_\beta) \sim 918$  keV, or ii)  $E_1, E_2$  are both within the  $\gamma$ -window and  $|E_{1(2)} - E_\gamma| < |E_{2(1)} - E_\gamma|$ . If both energies are outside the  $\gamma$ -window, arbitrarily the energy  $E_{1,2}$  with the lower DAQ channel number is used to populate the M2 histogram. Fig. 4 shows the resulting M2 histogram with the blue band indicating the  $\gamma$ -window, i.e. the region in which the search for the  $^{75}\text{As}$  de-excitation photon at 264.60 keV is performed: a  $\pm 12.5$  keV wide window around  $E_\gamma = 265$  keV. The width of this fit window was chosen sufficiently large both to contain the potential signal and to correctly model the background with a 1st order polynomial. Note that the choice made when  $E_1$  and  $E_2$  are both outside the  $\gamma$ -window has no effect on the nucleon-decay analysis that focuses on events within the  $\gamma$ -window. More details on the signal model and the systematic uncertainties related to the choice of the search window width are given in Sect. 4.1 and 4.4, respectively.

*Electron decay* For the analysis of the electron decay into  $\nu_e \gamma$ , a broadened  $\gamma$ -line signal has to be considered (see Sect. 2.3). Limiting the analysis to full energy  $\gamma$  peaks, the same M1 data set was used as for the bosonic DM analysis.

### 3.2 Detection efficiencies

To estimate the expected detection efficiencies, simulations were run in the MAJorana-GERda (MAGE) framework [28]. MAGE is a GEANT4-based software tool that allows users to generate simulated background and

signal histograms for the GERDA experiment. Separately for each detector type (Coax, BEGe, and IC), three different sets of particle emissions ( $e^-$ ,  $\gamma$ ,  $e^- + \gamma$ ) were simulated, as well as  $^{75}\text{Ge}$  decays. For all simulations, a set of  $10^7$  primary particles was generated, uniformly distributed over the detector array. Details on the simulation settings are reported in the following paragraphs. The generated raw files provide several pieces of information, e.g., the positions of the primary vertex, the hit energy depositions, and the particle types. The simulated events were then processed, taking into account specific settings for each experimental run, e.g., trigger thresholds, switched-off detectors, and dead layer models [29]. Acceptance efficiencies for the muon veto together with the quality cuts and the LAr veto were obtained as exposure-weighted averages of Phase II and II+ efficiencies [21]. For a given cut, the total acceptance efficiency is

$$\epsilon_{\text{cut}} = \frac{1}{\mathcal{E}} (\epsilon_{\text{cut, II}} \cdot \mathcal{E}_{\text{II}} + \epsilon_{\text{cut, II+}} \cdot \mathcal{E}_{\text{II+}}). \quad (13)$$

Using exposures  $\mathcal{E}_{\text{II}} = 61.4$  kg yr and  $\mathcal{E}_{\text{II+}} = 44.1$  kg yr, total cut efficiencies of  $\epsilon_\mu = 0.999(1)$  and  $\epsilon_{\text{LAr}} = 0.979(1)$  were obtained for the muon and LAr veto, respectively. The total detection efficiency for a given final state  $x$  is computed as

$$\epsilon_x = \epsilon_\mu \cdot \epsilon_{\text{LAr}} \cdot \sum_{i=1}^{N_d} \frac{\mathcal{E}_i \cdot \epsilon_{x,i}}{\mathcal{E}}, \quad (14)$$

where  $\mathcal{E}_i$  and  $\epsilon_{x,i}$  are the exposure and the efficiency for detector  $i$  and data set  $x$ , respectively.  $N_d$  denotes the total number of data sets. The full exposure  $\mathcal{E}$  was divided into five data sets: enr-BEGe (32.8 kg yr) and enr-Coax (28.6 kg yr) from Phase II, plus enr-BEGe (22.2 kg yr), enr-Coax (13.2 kg yr) and enr-IC (8.7 kg yr) from Phase II+. Table 2 provides a summary of the total detection efficiencies  $\epsilon_x$  for the potential signals in our search for new physics. More details are given below for each simulated process. For all simulated efficiencies, the statistical uncertainty is negligible given the high number of simulated events. The dominant systematic uncertainties affecting the efficiencies are the detectors' active volume uncertainties. For the nucleon decay search, there is an additional systematic uncertainty coming from the  $^{76}\text{Ge}$  enrichment level uncertainty. Systematic uncertainties are further commented in Sect. 4.4. Summing in quadrature all contributions, a total uncertainty of 5% is accounted in all searches.

*Bosonic DM* Simulations of electron energies in the interval 65 to 1021 keV are required for the bosonic DM absorption channel, while for the dark Compton scattering channel the simulation of electrons and photons

**Table 2** Summary of total detection efficiencies for indicated searches of potential signals from new physics. Quoted uncertainties include a total systematic uncertainty of 5%; the statistical contributions can be neglected given the high number of simulated primaries

<b>Bosonic DM</b>	
electron, $\epsilon_{e^-}$	
65 keV	$0.852 \pm 0.043$
1021 keV	$0.805 \pm 0.040$
electron & photon, $\epsilon_{e^- \wedge \gamma}$	
65 keV	$0.839 \pm 0.042$
1021 keV	$0.165 \pm 0.008$
<b>Nucleon decay via <math>^{75}\text{Ge}</math> decay</b>	
coincidence of electron & 264.60 keV photon, $\epsilon_n$	$0.0020 \pm 0.0001$
<b>Electron decay</b>	
$m_e/2$ keV $\gamma$ -ray emitted	
within recording detector, $\epsilon_{\text{Ge,det}}$	$0.419 \pm 0.021$
by neighbouring Ge material, $\epsilon_{\text{Ge,mat}}$	$0.034 \pm 0.002$
by LAr, $\epsilon_{\text{Ar}}$	$0.00070 \pm 0.00004$

in the final state is needed. Starting at 65 keV, efficiencies were computed as the ratio between the number of events in the full-energy peak and the number of simulated particles in steps of 1 keV. Primaries were simulated separately for each phase (Phase II or Phase II+) and detector type. The total detection efficiencies were calculated as exposure-weighted means for the entire data-taking time and overall detector types (see Eq. (14)). Including acceptance efficiencies for quality cuts, muon veto and LAr veto, total detection efficiencies for tagging electrons range from  $0.852 \pm 0.043$  at 65 keV to  $0.805 \pm 0.040$  at 1021 keV. The same energy grid was used for the total energy when generating electrons plus photons from a single vertex with the energy constraints given by Eq. (6). Including all cuts, total detection efficiencies for tagging simultaneously electrons and photons at energy  $T + \omega' = m_{DM}$  range from  $0.839 \pm 0.042$  at 65 keV to  $0.165 \pm 0.008$  at 1021 keV. At higher energies, the efficiency rapidly decreases because the probability of losing photons gets higher. In the window 65-1021 keV, the  $\gamma$  attenuation length in Ge material ranges from  $\mathcal{O}(\text{mm})$  up to  $\mathcal{O}(\text{few cm})$  for energies above  $\sim 100$  keV [4, 30]. Escaping photons deposit energy either outside Ge material (if in LAr, the full event is discarded), leading to electron only signals at energy  $T < m_{DM}$ , or in a second germanium detector, leading to M2 events that are discarded from the bosonic DM analysis.

*Nucleon decays via  $^{75}\text{Ge}$*  Applying the same energy cuts used for building the M2 data set (see Sect. 3.1), the  $\beta$  decay of  $^{75}\text{Ge}$  and the subsequent gamma decays in  $^{75}\text{As}$  were simulated as well. Weighting over individual data sets with their exposures, a total detection efficiency of  $0.0020 \pm 0.0001$  was derived.

*Electron decay* The detection efficiency of measuring a  $\sim 256$  keV photon released after the electron decay in the Ge detectors and LAr volume was separately simulated. The efficiency, averaged over the exposure and accounting for the applied cuts, is found to be  $0.419 \pm 0.021$  for decays recorded in germanium detectors and  $0.034 \pm 0.002$  for decays originating from detectors surrounding the one that fully recorded the outgoing photon. The efficiency of tagging photons originating in LAr was found to be  $(7.0 \pm 0.4) \times 10^{-4}$ . This contribution was simulated in a cylinder with a radius of 0.8 m and a height of 1.4 m shielding the detector array, for a total mass of  $m_{\text{Ar}} = 3884.1$  kg.

## 4 Analysis methods

### 4.1 Signal model

In all signal channels searched for, full energy depositions within the Ge detectors are assumed, leading to peaks above the background continuum. The expected line at a probed energy would be constrained by the finite energy resolution of the detectors. The signal shape was thus modelled as a Gaussian profile under the assumption of a symmetric line shape for full charge collections. In the case of the electron decay channel, the line would be further broadened because of the Doppler effect as described in Sect. 2.3. Given that all data were merged over different detector channels, the signal shape was a mixture of individual Gaussian distributions for each detector. The energy resolution (in standard deviations of a Gaussian peak) within different detector types operated in GERDA agree very well on the order of  $\mathcal{O}(1 \text{ keV})$ , with systematic uncertainties of approximately 0.1-0.2 keV, which comply with the systematic uncertainty on the energy scale [31]. The exposure-weighted resolution  $\sigma$  ranges from 0.9 keV up to 1.2 keV in the bosonic DM interval of interest of 65 keV to  $2m_e$ . For particle disappearances at  $\sim 265$  keV and  $\sim 256$  keV, the energy resolution  $\sigma$  is 0.9 keV. A bin size of 1 keV was thus chosen, being the closest integer to the energy resolution in standard deviations. Compared to this width, the uncertainties mentioned above are sufficiently small to accurately model the peak shape via a Gaussian mixture model over detector types, instead of using a full mixture model over all



individual detector channels. The weights in the mixture model are the exposures of the individual detector types, as well as the two data-taking phases. Both signal centroid and resolution, as measured from approximately weekly calibrations [31], were fixed for every probed signal model, leaving only the signal strength amplitude as a free parameter in the signal shape to be fitted.

For a DM signal model, the search window was limited to 25 keV, centred at the incoming DM mass particle, which is sufficiently large to compare the potential signal with  $\sim 1$  keV resolution in standard deviations to the wide background continuum discussed below. Every integer mass value in the search range of  $65-2m_e$  keV was probed iteratively. For the nucleon decay, the same search window width was used but evaluated for the coincident M2 data centred at  $E_\gamma \sim 265$  keV. For the electron decay channel, owing to the broadening, the search window was increased to a width of 120 keV, ranging from 196 keV to 316 keV.

## 4.2 Background model

*Background continuum* The GERDA background model after the LAr veto cut does not fully cover the energy range of interest [32]. Hence, it does not reproduce the observed  $^{39}\text{Ar}$  dominated spectral shape at lower energies. Thus, an empirical fit model, motivated by the underlying physical processes, was applied to constrain the background continuum in the M1 data set. The  $2\nu\beta\beta$ -decay dominated upper half of the signal range was modelled with a polynomial function. The dominating  $^{39}\text{Ar}$   $\beta$ -decay background contribution at energies below approximately 500 keV was modelled with a modified  $\beta$ -decay distribution [33, 34]. Owing to the propagation of the emitted electrons through the cryogenic liquid, resulting in strong bremsstrahlung emissions, a modification to the original  $\beta$ -decay shape was needed. Plots of the empirical background model as applied for the signal search, and an evaluation of its accuracy to describe the data, are provided in the Appendix (see Sect. B).

No background decomposition of the M2 energy spectrum shown in Fig. 4 is available. These events have a different energy distribution compared to M2 data shown in [35]. The difference comes from having applied both an energy cut to M2 events and the LAr veto in this paper. Moreover, the M2 spectrum used in [35] contains the sum of the two coincident energies. The  $\gamma$  energy spectrum was instead fitted with a linear function of energy in a 25 keV wide interval around the expected signal at  $\sim 265.0$  keV.

*$\gamma$ -ray background* Background  $\gamma$ -radiation emitted from surrounding materials creates the very same peak profile in the data as the bosonic DM signals searched for. Thus, the  $\gamma$ -lines cannot be distinguished from these signals. Hence, as a first step, a generic search for any peak-like excess above the background continuum was performed, independently of whether an excess was caused by a known isotope transition or new physics. If the significance of an excess exceeded  $3\sigma$ , and if it could be explained by a known  $\gamma$ -transition, the corresponding  $\gamma$ -line peak was added to the background model. When evaluating limits on the bosonic DM interactions and the electron decay lifetime, the background model function was refitted in a second step, including the  $\gamma$ -rays identified during the generic search. When determining bosonic DM limits, the  $\gamma$ -line peak energies were excluded together with 3 bins on the right and on the left, corresponding to an exclusion window of approximately 2.5 FWHM width for each detected  $\gamma$  line.

## 4.3 Statistical frameworks

Two independent statistical analyses were conducted to identify a potential excess at any probed energy value. A binned Bayesian fit of the signal peak above the background model was performed in the respective signal window, employing a positive uniform prior for the signal strength amplitude. In addition, a Frequentist fitting procedure was employed using the profile likelihood-ratio test statistics from [36]. Asymptotic distributions were assumed to hold, and the physically allowed signal strength was constrained to the positive domain. Both statistical approaches are described in more detail in the Appendix (see Sect. C). In both methods, a  $3\sigma$  threshold was required to identify an indication of a potential signal. A  $4\sigma$  effect was required to claim signal evidence in the particle decay searches, a  $5\sigma$  effect in the bosonic dark matter search which is prone to a strong look-elsewhere effect as discussed in Sect. C. An example of a Bayesian fit is shown in Fig. 5 at the potential mass of 662 keV for which an excess of  $5.1\sigma$  has been observed and attributed to the known  $^{137}\text{Cs}$  line at  $\sim 662.0$  keV. The observed local  $p$ -values for each probed peak position in the bosonic DM search range, as determined in the Frequentist framework, are shown in Fig. 6. Overall, nine expected  $\gamma$ -ray transitions were identified, plus one unknown excess at 710 keV, as listed in Table 3. The global significance of the unidentified excess is discussed in the Appendix (see Sect. C). As the corresponding local significance of this peak remains below the evidence threshold, it was concluded that no bosonic DM signal was found.

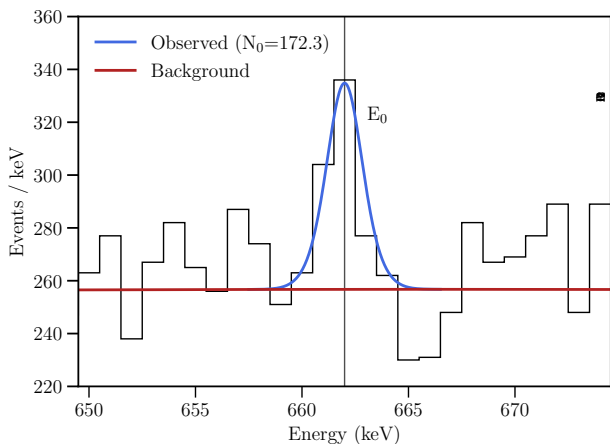


**Fig. 5** Part of the M1 spectrum shown in Fig. 3 with an example of a Bayesian fit at 662 keV (vertical line). The empirical background contribution is shown in red, while the best-fit model is shown in blue.  $N_0$  denotes the best-fit signal strength. The signal excess of  $5.1\sigma$  can be explained by the 661.7 keV  $\gamma$ -line from  $^{137}\text{Cs}$  (see Table 3)

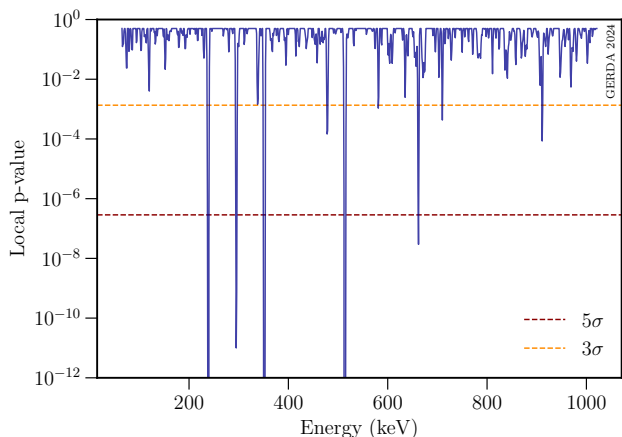


**Fig. 6** Plot of the local p-values of all count strength amplitudes versus the tested energies for the DM search. Apart from the  $3\sigma$  excess at 710 keV all other local excesses with  $\geq 3\sigma$  can be attributed to known  $\gamma$  transitions (see Table 3)

Also for the nucleon and electron decay channels no significant signal excess was seen. Hence, upper limits were evaluated for all new physics searches independently at 90% CI and 90% CL (see Sect. C for technical details). The corresponding sensitivities were determined via Monte Carlo (MC) simulations in the Bayesian case, and via Asimov data sets [36] in the Frequentist method.

**Table 3** List of energy ranges  $R$  where  $\geq 3\sigma$  excesses are found by the Bayesian and/or Frequentist fits, and their maximum significance  $S$  (Bayesian, Frequentist). The most likely origin of these peaks are  $\gamma$  transitions from indicated nuclei; the respective energies  $E_\gamma$  are taken from [37]

$R$ (keV)	$S$ ( $\sigma$ )	Origin	$E_\gamma$ (keV)
237 - 240	8.4, 8.5	$^{212}\text{Pb}$	238.632 (2)
293 - 297	6.4, 6.7	$^{214}\text{Pb}$	295.224 (2)
338	2.9, 3.0	$^{228}\text{Ac}$	338.320 (5)
349 - 353	10.0, 10.7	$^{214}\text{Pb}$	351.932 (2)
477 - 479	3.6, 3.6	$^{228}\text{Ac}$	478.4 (5)
512 - 516	8.8, 10.2	$^{85}\text{Kr}$	513.997 (5)
581	3.1, 3.1	$^{208}\text{Tl}$	583.187 (2)
660 - 663	5.1, 5.4	$^{137}\text{Cs}$	661.657 (3)
710	2.9, 3.3	-	-
910 - 912	3.5, 3.8	$^{228}\text{Ac}$	911.196 (6)

#### 4.4 Systematics

Different sources of systematic uncertainties were investigated. In the Bayesian framework, the accuracy of expected limits was checked via MC simulations. At each probed energy value,  $10^3$  toy-MC spectra were generated assuming no signal and Poisson fluctuations for the number of background events. Each toy spectrum was fitted with a signal+background model. The distribution of the derived limits for the signal strength amplitudes was used to derive the median sensitivity. Measured limits are well contained within the simulated expectation bands and agree with the median sensitivity expected in case of no signal (see Fig. 12 in Appendix E). In the Frequentist case, the Asimov data sets were employed to investigate systematic uncertainties. Here both the accuracy of the Asimov sensitivity estimations and the assumption of asymptotic distributions for the limit evaluation were confirmed via  $10^6$  MC simulations at the equally spaced energies  $\{100, 150, \dots, 1000\}$  keV for bosonic DM searches and at the energies of the nucleon and electron decay channel. The resulting uncertainties are within 11 (3)% for the M2 (M1) data set, which is judged sufficiently accurate. The systematic uncertainty on the bosonic DM results caused by the background modelling approach was checked via a different background fit. The results obtained with the empirical background fit model were compared to those obtained with a polynomial background continuum fit in each individual search window, in exact analogy to our former work shown in [2]. The respective sensitivities reveal a systematic uncertainty of  $\sim 1\%$ , indicating a good accuracy of the background modelling procedure. Here, the uncertainty was estimated as the median of all deviations between the two approaches. Following the same fitting treatment as in our previous

work would change the Bayesian (Frequentist) limits by approximately 1 (2)%, again estimated as the median deviation.

The impact of modelling the background continuum on the results for the electron (nucleon) decay channel was probed as well, using a second (first) order polynomial function and different search window widths. The differences in the Bayesian (Frequentist) sensitivities for different fitting strategies remain within approximately 2 (4)% for the nucleon decay analysis and are  $\sim 1\%$  for the electron decay search.

Furthermore, the effect of the bin width has been investigated. Probing bin widths within reasonable proximity to the energy resolution scale in standard deviations of 1 keV, with a systematic uncertainty of around 0.1-0.2 keV, reveals an uncertainty on both bosonic DM results of  $\sim 7\%$ . The uncertainties are slightly smaller for the decay channel sensitivities, independently of the statistical framework.

The detector-geometry-related uncertainties caused by the active volume or the level of enrichment in  $^{76}\text{Ge}$  (the latter being relevant for the nucleon decay search only) have an impact of approximately 4% and 2%, respectively. These were estimated as the exposure-weighted mean of the active volume and enrichment fraction uncertainties of the different detector types [21].

## 5 Results

### 5.1 Bosonic dark matter

No evident excess caused by bosonic DM interactions has been found beyond the expected fluctuations of the continuous background. Using the interaction rate formulas shown in Sect. 2.1, the derived count strength limits  $N_{\text{up}}$  at 90% CI and CL are converted into upper limits on the maximal physical interaction strength of ALPs and the kinetic mixing of DPs. In particular, the conversion formula reads

$$g_\phi = \frac{N_{\text{up}}}{\mathcal{E}_{1(2)} \cdot 365.25 \cdot R_\phi}, \quad (15)$$

where  $\phi$  denotes the DM candidate of interest, which can either be an ALP ( $\phi \equiv a$  and  $g_\phi \equiv g_{ae}^2$ ) or a DP ( $\phi \equiv V$  and  $g_\phi \equiv \alpha'/\alpha$ ), and  $\mathcal{E}_{1(2)}$  the exposure of 60.0 or 105.5 kg yr (see Table 1). The total DM interaction rate  $R_\phi$  ( $\text{kg}^{-1}\text{d}^{-1}$ ) accounting for detection efficiencies shown in Table 2 is given by

$$R_\phi = \epsilon_{e^-} \cdot R_\phi^A + \epsilon_{e^- \wedge \gamma} \cdot R_\phi^C. \quad (16)$$

When computing the absorption interaction rates through Eqs. (4) and (5), the photoelectric cross-section  $\sigma_{\text{pe}}$  for

germanium target material was taken from Ref. [27]. The molar mass  $M_{\text{tot}} = 75.66$  g/mol of enriched Ge detectors was computed as

$$M_{\text{tot}} = f_{^{76}\text{Ge}} \cdot M_{^{76}\text{Ge}} + (1 - f_{^{76}\text{Ge}}) \cdot M_{\text{res}}, \quad (17)$$

where the GERDA exposure-weighted  $^{76}\text{Ge}$  enrichment fraction is  $f_{^{76}\text{Ge}} = 87.5\%$  [21]. The molar mass of all isotopes but  $^{76}\text{Ge}$  present in enriched Ge detectors is computed as

$$M_{\text{res}} = \sum_{i \neq 76} \frac{M_i \cdot f_i}{f_{\text{tot}}}, \quad (18)$$

for Ge isotopes  $i = \{70, 72, 73, 74\}$ . Molar masses  $M_i$  are taken from [27], while relative isotopic composition values  $f_i$  were taken from Table 1 of [21], with  $f_{\text{tot}} = \sum_{i \neq 76} f_i$ . In particular,  $M_{^{76}\text{Ge}} = 75.92$  g/mol and  $M_{\text{res}} = 73.86$  g/mol. The derived limits on the kinetic mixing strength of DPs and the ALP-electron coupling are compared to other experimental results in Fig. 7. Constraints for specific masses are listed in the Appendix, see Table 7 in Sect. D. The results obtained with the Frequentist method largely align with the Bayesian results, but are slightly more stringent at the locations of underfluctuations below the expected background levels. In the Appendix, individual effects of the absorption and the scattering process on the total results are shown (see Sect. D), and the sensitivities compared as determined with the two different statistical approaches (see Sect. E).

The new limits derived by GERDA are among the most stringent direct measurement results between  $\sim 140$  keV and  $2m_e$ , if not the best. Better constraints are reported only for masses in the intervals of about 245-280 keV and 570-670 keV by COSINE-100 [43]. Comparing old [2] and new GERDA limits improvements of almost up to two orders of magnitude are achieved at energies above  $\sim 500$  keV for the DP channel due to the domination of the Compton cross-section versus the absorption cross-section. For ALPs, this corresponds to an improvement of almost one order of magnitude. At intermediate energies, the doubled exposure in combination with the combined effect of absorption and scattering leads to about 2 to 10 times more severe constraints, depending on the precise energy and the particle candidate. At lower energies, the new results improve only marginally upon the limits derived in [2]. The small improvement in this region is mostly triggered by an approximately four times higher exposure, meaning an expected improvement by a factor of 2 only, as the dark Compton process does not contribute relevantly in this range. Hence, the sensitivities of xenon-based direct DM detection experiments could not be reached,

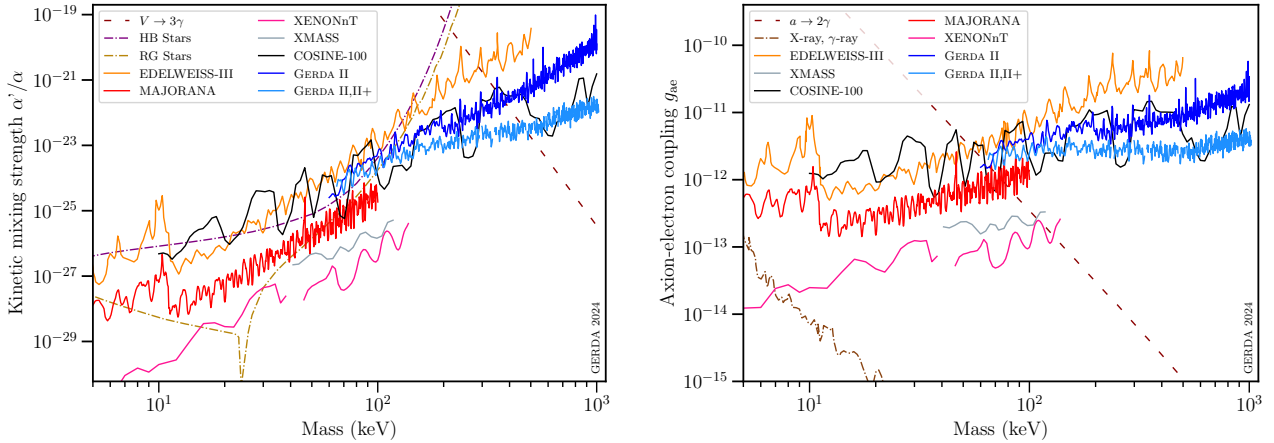


**Fig. 7** Bayesian exclusion limits on bosonic DM couplings to electrons obtained from GERDA Phase II and Phase II+ data (light blue line). The limits were deduced by converting the upper count strength limits into physics constraints including in the interaction rate both the photoelectric-like absorption and the dark Compton scattering processes, see Eq. (15). The regions around identified  $\gamma$ -lines (see Table 3 and numerical data in Supplemental Material [38]) have been omitted. Left: Bayesian constraints at 90% CI on the kinetic mixing strength of DPs. Right: Bayesian constraints at 90% CI on the coupling strength of ALPs to electrons. Results from other direct detection experiments [39–43] are shown, as well as the previous GERDA limits [2]. Note that in the COSINE-100 paper [43] the previous numerical factors of 1.2 and 4 have been used in eqs. 4 and 5. The dashed, dark red line indicates the region below which the interpretation as a DM candidate being stable on the scale of the age of the Universe is valid without further assumptions [9]. Indirect constraints from X-ray and  $\gamma$ -ray observations taken from Refs. [9, 44] are indicated by the dot-dashed, brown line. Constraints derived from red giant (RG, dot-dashed, gold line) and horizontal branch (HB, dot-dashed, purple line) star energy losses are discussed in [45]

due to the higher background level in our low energy range and the lower exposure.

## 5.2 Nucleon decays

A lower constraint on the nucleon lifetime based on the observed upper limit on the event number  $N_{\text{up},n}$  is calculated as

$$\tau_{\text{low}} = \epsilon_n \cdot N_{\text{eff}} \cdot \frac{N_A}{N_{\text{up},n}} \cdot \mathcal{E} \cdot \frac{f_{76\text{Ge}}}{M_{\text{tot}}} \quad (19)$$

where  $\epsilon_n$  is the efficiency to tag a coincident electron-photon pair (see Table 2 in Sect. 3),  $N_{\text{eff}}$  is the effective number of particles which can undergo the considered decay, and  $N_A$  is the Avogadro’s constant.  $M_{\text{tot}}$  (kg/mol) and  $f_{76\text{Ge}}$  are given in Sect. 5.1, while the exposure  $\mathcal{E} = 105.5$  kg yr is taken from Table 1. As described in Sect. 2.2, only one specific branch of the inclusive nucleon decay is considered, i.e. the one in which the nucleon decays from one of the most external nuclear shells with the de-excitation of the daughter nucleus by  $\gamma$ -emission only, without subsequent emission of other particles. Hence, it is necessary to know the effective number of decaying neutrons (protons) inside the parent  $^{76}\text{Ge}$  nuclei, whose decay could produce the specific daughter nucleus  $^{75}\text{Ge}$  ( $^{75}\text{Ga}$ ). Following Refs. [46–49], the effective number  $N_{\text{eff}} = 16$  (14) for

neutrons (protons) was obtained by using the single-particle shell model with a modified Woods-Saxon potential [50, 51], and the set of parameters adjusted for  $^{76}\text{Ge}$ . The calculations were done with the shell-model codes KSHELL [52] and CoSMo [53] comparing, where possible, our full range of the sub-shell nucleon binding energies with the values obtained in Refs. [54, 55].

In the Bayesian framework a best fit of 6.8 counts was obtained, with a significance of  $1.1\sigma$  (see Fig. 8). The 90% CI upper limit is equal to  $N_{\text{up},n} = 16.5$  counts, and the median sensitivity is estimated to be  $N_{\text{s},n} = 10.5$  counts. In the Frequentist approach, the best-fit signal strength is 4.2 counts, corresponding to a significance of  $0.7\sigma$ . This leads to a count limit of  $N_{\text{up},n} = 15.2$  counts with a median sensitivity estimate of  $N_{\text{s},n} = 9.8$  counts. The respective limits on the nucleon lifetimes estimated through Eq. (19) are shown in Table 4. The lifetime limit for  $N_{\text{eff}} = 1$  is provided both as a measure of the inclusive *nuclear* decay rate and for comparison with other published limits, where different effective numbers of nucleons were used depending on the specific isotopes under consideration.

For a comparison with the results of previous nucleon disappearance studies see the detailed compilation of the Particle Data Group ‘p Mean Life’ [56]. For inclusive decays of neutrons and protons bound in  $^{129,136}\text{Xe}$  [46, 47],  $^{127}\text{I}$  [48] and  $^{130}\text{Te}$  [49, 57] mean

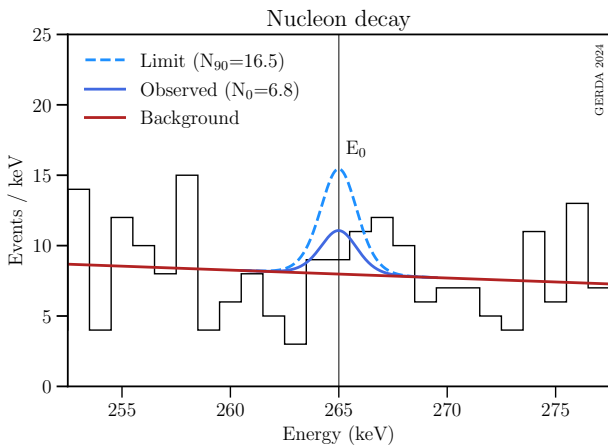


**Fig. 8** Part of the M2 spectrum shown in Fig. 4 with the Bayesian fit of the nucleon decay signal at  $E_0 \sim 265$  keV. A 1st-order polynomial was used to model the continuous background

life limits between  $3.3 \times 10^{23}$  and  $8.6 \times 10^{24}$  yr have been found. Orders of magnitude better limits are reported by the Borexino, KamLAND and SNO+ collaborations for the parent nuclei  $^{12,13}\text{C}$  [58, 59] and  $^{16}\text{O}$  [60] profiting from the huge mass of their low-background detectors. These latter experiments provide limits on the decay of bound nucleons into invisible modes where no energy is deposited in the detector in the decay itself. The best limits are provided by SNO+ for neutron and proton disappearance in  $^{16}\text{O}$ ,  $9 \times 10^{29}$  yr and  $9.6 \times 10^{29}$  yr, respectively [60].

### 5.3 Electron decay

Similarly to Eq. (19), the constraint on the electron decay lifetime is calculated as

$$\tau_{\text{low}} = (\epsilon_{\text{Ge,det}} + \epsilon_{\text{Ge,mat}}) \cdot N_{\text{e,Ge}} \cdot \frac{N_{\text{A}}}{N_{\text{up,e}}} \cdot \frac{\mathcal{E}}{M_{\text{tot}}} + \epsilon_{\text{Ar}} \cdot N_{\text{e,Ar}} \cdot \frac{N_{\text{A}}}{N_{\text{up,e}}} \cdot \frac{m_{\text{Ar}}}{m_{\text{Ge}}} \cdot \frac{\mathcal{E}}{M_{\text{Ar}}}. \quad (20)$$

Here  $N_{\text{e,Ge}} = 32$  and  $N_{\text{e,Ar}} = 18$  are the numbers of electrons in Ge and Ar atoms. The LAr molar mass is  $M_{\text{Ar}} = 39.95 \times 10^{-3}$  kg/mol, with total mass  $m_{\text{Ar}} = 3884.1$  kg. The total Ge mass  $m_{\text{Ge}} = 38.78$  kg is computed as exposure-weighted averages of Phase II and II+ masses [21]. Exposure  $\mathcal{E} = 105.5$  kg yr and efficiencies are taken from Table 1 and 2, respectively.  $M_{\text{tot}}$  (kg/mol) is given in Sect. 5.1.

For the 255.9 keV Doppler broadened  $\gamma$ -line caused by a potential electron decay in Ge or Ar, no relevant deviation from the expected background was observed in the

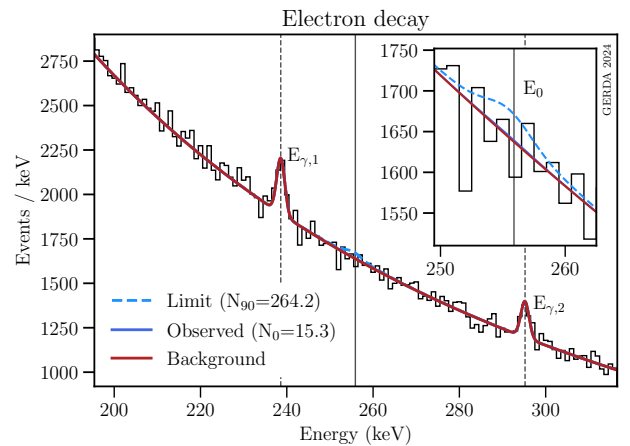


**Fig. 9** Part of the M1 spectrum shown in Fig. 3 with the Bayesian fit of the electron decay at  $E_0 = 255.9$  keV (continuous line). The background fit includes two significant  $\gamma$ s (dashed lines) at  $E_{\gamma,1} = 238.6$  keV ( $^{212}\text{Pb}$ ) and  $E_{\gamma,2} = 295.2$  keV ( $^{214}\text{Pb}$ ), see Table 3

data. In the Bayesian fitting method, shown in Fig. 9, the best-fit amplitude equals 15.3 counts with significance equal to  $0.3\sigma$ . The obtained limit is  $N_{\text{up,e}} = 264.2$  counts, and the median sensitivity is  $N_{\text{s,e}} = 249.4$  counts. In the Frequentist procedure, a best-fit value of 3.8 counts is found, with vanishing significance. The evaluation of the upper limit yields  $N_{\text{up,e}} = 263.1$  counts, with a sensitivity of  $N_{\text{s,e}} = 259.2$  counts. The corresponding limits on the electron lifetime are listed in Table 4, and set into perspective in Table 5. The liquid-scintillator experiment Borexino set the currently tightest constraint. All other results were obtained with Ge detectors. Note that the validity of the statistical analysis conducted to obtain the numerical value of [18] has been questioned in Refs. [56, 61].

## 6 Conclusions and outlook

In this paper, searches for full energy depositions caused by a coupling of bosonic DM with keV-scale masses with the atoms in the GERDA detectors are reported. No significant excess has been observed, hence constraints on the kinetic mixing of DPs as well as on the coupling of ALPs to electrons have been derived, in both Bayesian and Frequentist frameworks. Furthermore, the stability of the neutron and the proton inside  $^{76}\text{Ge}$  against inclusive decays with subsequent  $\gamma$ -only emission of the daughter isotope has been investigated by searching for a coincident signal induced by a  $^{75}\text{Ge}$   $\beta$  decay accompanied by the dominating  $^{75}\text{As}$  de-excitation  $\gamma$ -line of 264.60 keV. In addition, a Doppler

**Table 4** Summary of results of the search for inclusive neutron ( $n$ ) and proton ( $p$ ) decays ( $n, p \rightarrow X$ ) in  $^{76}\text{Ge}$  as well as for electron decay  $e^- \rightarrow \nu_e \gamma$ . For each decay, the observed best-fit value (*obs.*) is shown together with its significance (*sig.*). The extracted upper limits at 90% CI/CL and the median sensitivity for the signal strength are indicated with  $N_{\text{up}}$  and  $N_s$ , respectively. Lower lifetime limits ( $L$ ) on  $\tau_{\text{low}}$  are deduced in the Bayesian and Frequentist frameworks according to Eqs. (19), (20) at 90% CI and CL, respectively, with the sensitivity  $S$  equal to the median value assuming the background-only hypothesis.  $N_{\text{eff}} = 16$  (14) denotes the effective numbers of neutrons (protons) used for deriving the nucleon lifetime limit.  $N_{\text{eff}} = 1$  yields the corresponding nuclear decay rate limit. As to electron decay,  $N_{\text{eff}}$  denotes the number of electrons in Ge and Ar atoms

Search	Framework	Signal counts			$N_{\text{eff}}$	$\tau_{\text{low}}(\text{yr})$	
		<i>obs. (sig.)</i>	$N_{\text{up}}$	$N_s$		$L$	$S$
$n, p \rightarrow X$	Bayesian	6.8 (1.1 $\sigma$ )	16.5	10.5	1	$9.1 \times 10^{22}$	$1.4 \times 10^{23}$
					16 ( $n$ )	$1.5 \times 10^{24}$	$2.3 \times 10^{24}$
					14 ( $p$ )	$1.3 \times 10^{24}$	$2.0 \times 10^{24}$
	Frequentist	4.2 (0.7 $\sigma$ )	15.2	9.8	1	$9.8 \times 10^{22}$	$1.5 \times 10^{23}$
					16 ( $n$ )	$1.6 \times 10^{24}$	$2.4 \times 10^{24}$
					14 ( $p$ )	$1.4 \times 10^{24}$	$2.1 \times 10^{24}$
$e^- \rightarrow \nu_e \gamma$	Bayesian	15.3 (0.3 $\sigma$ )	264.2	249.4	32 (Ge), 18 (Ar)	$5.4 \times 10^{25}$	$5.7 \times 10^{25}$
	Frequentist	3.8 (0.0 $\sigma$ )	263.1	259.2	32 (Ge), 18 (Ar)	$5.4 \times 10^{25}$	$5.5 \times 10^{25}$

**Table 5** Selection of constraints on the electron lifetime  $\tau_e$  at 90% CL

Experiment	Nuclei	Decay	$\tau_e(\text{yr})$
Borexino [62]	C, H, N, O	$e^- \rightarrow \nu_e \gamma$	$6.6 \times 10^{28}$
HdM [18] <sup>(a)</sup>	Ge	$e^- \rightarrow \nu_e \gamma$	$9.4 \times 10^{25}$
MAJORANA [63]	Ge	$e^- \rightarrow 3\nu_e$	$2.8 \times 10^{25}$
EDELWEISS-III [39]	Ge	$e^- \rightarrow 3\nu_e$	$1.2 \times 10^{24}$
GERDA	Ge	$e^- \rightarrow \nu_e \gamma$	$5.4 \times 10^{25}$

<sup>(a)</sup> more likely overestimate [56, 61]

broadened  $\gamma$ -line at 255.9 keV, which would be induced by the charge non-conserving decay of an electron into  $\nu_e \gamma$ , has been analysed. None of the particle disappearance modes has been found, and constraints on the lifetimes of these particles have been derived in both statistical frameworks.

The limits for the search of DP and ALP DM pose the most stringent direct experimental results between roughly 140 keV and  $2m_e$ , except for masses in the 245-280 keV and 570-670 keV intervals where stronger constraints are set by COSINE-100 [43]. However, for vector DM candidates, the indirect lifetime constraint based on the age of the Universe dominates significantly over the derived limits for masses above  $\sim 500$  keV. In general, indirect galactic background searches for  $3\gamma$  induced by DP decay are significantly more stringent [64]. In the energy range studied by GERDA, ALP DM models are mostly constrained by indirect, astrophysical measurements. Moreover, the ALP masses are further largely ruled out by the needed stability over the age of the Universe if one again assumes ALPs to

compose the entire DM [9]. The results for the ALP channel are shown as well, as more exotic, fine-tuned models have been suggested therein to omit the latter constraint. As a further remark, direct constraints on the absorption of ALPs have been reinterpreted to probe violations of Poincaré invariance [65]. Hence, not only all combined results for ALPs and DPs, but also the individual absorption and the scattering channel constraints, are appended to this paper (see Fig. 11).

Regarding the determined lower lifetime limits on the inclusive nucleon decays in  $^{76}\text{Ge}$ , it is emphasised that, to our knowledge, these are the first constraints on these processes in  $^{76}\text{Ge}$ . However, the sensitivity of GERDA compared to the free nucleon decays or mode-dependent decays in any isotope is orders of magnitude below that reached by large-scale experiments with light nuclei [58–60]. The electron lifetime limit is among the strongest limits measured with semiconductor detectors, although the sensitivity does not reach that of large-scale organic scintillation experiments such as Borexino [66].

The analyses presented here motivate further searches for these new physics channels with  $\mathcal{O}(100\text{ keV})$  energy depositions in semiconductor experiments. In particular, the future LEGEND-1000 experiment, aiming at the operation of more than one tonne of Ge detectors enriched in  $^{76}\text{Ge}$  for ten years in underground-sourced LAr [67], will improve these Ge-based constraints on bosonic DM interactions and lifetimes of electrons, neutrons, and protons. The  $^{39}\text{Ar}$  concentration in underground-sourced LAr is measured by the DarkSide collaboration to be reduced by a factor 1400 [68]. Thus the sensitivity of LEGEND-1000 will be enhanced in the low-energy regime by more than an order of mag-

nitude. Further improvements could be realised by deploying Ge detectors of natural isotopic composition (or depleted in  $^{76}\text{Ge}$ ) in a setup similar to LEGEND-1000, to reduce the background induced by  $2\nu\beta\beta$  decays.

**Acknowledgements** The GERDA experiment is supported financially by the German Federal Ministry for Education and Research (BMBF), the German Research Foundation (DFG), the Italian Istituto Nazionale di Fisica Nucleare (INFN), the Max Planck Society (MPG), the Polish National Science Centre (NCN, Grant number UMO-2020/37/B/ST2/03905), the Polish Ministry of Science and Higher Education (MNiSW, Grant number DIR/WK/2018/08) the Russian Foundation for Basic Research, and the Swiss National Science Foundation (SNF). This project has received funding and support from the European Union’s Horizon 2020 research and innovation programme under the Marie Skłodowska-Curie Grant Agreements No. 690575 and No. 674896. This work was supported by the Science and Technology Facilities Council, part of the U.K. Research and Innovation (Grant No. ST/T004169/1). The institutions acknowledge also internal financial support. The GERDA collaboration thanks the directors and the staff of LNGS for their continuous strong support of the GERDA experiment.

**Data Availability** This manuscript has associated data in a data repository. [Authors’ comment: The data shown in Figs. 3, 4 and 7 is available in ASCII format as Supplemental Material [38].]

## Appendix

### A: Doppler broadened peak profile

Using the virial theorem, i.e.  $E_{\text{kin.}} = -E_{\text{pot.}}/2$ , the Doppler broadened line shape can be analytically described as a sum of Gaussian contributions over all atomic shells weighted by their electron occupancy number  $n_i$ ,

$$I(E) = \sum_{i=1}^{N_b} I_i(E) = \sum_{i=1}^{N_b} \frac{n_i}{\sqrt{2\pi}\sigma_i} e^{-\frac{(E-E_{t,i})^2}{2\sigma_i^2}}, \quad (\text{A.1})$$

where  $N_b$  is the total number of atomic shells for a given atom [18] and  $E_{t,i}$  is the total energy deposited in a detector after an electron decay (see Eqs. (11) and (12)). The line width for the  $i$ -th atomic shell is

$$\sigma_i = E_{t,i} \cdot \sqrt{\frac{k_B T_i}{m_e}} \approx 0.0442 \cdot E_{t,i} \cdot \sqrt{E_{b,i}}, \quad (\text{A.2})$$

where  $k_B$  is Boltzmann’s constant and  $T_i$  is the absolute electron temperature, with energies  $E_{t,i}$  and  $E_{b,i}$  expressed in keV. Notice that the numerical pre-factor has been found upon recalculation, whereas [18] states a slightly larger value of 0.0447. The individual Ge and Ar atomic shell contributions as deduced from their respective electron binding energies are listed in Table 6.

**Table 6** Germanium and argon electron binding energies  $E_{b,i}$  for different atomic shells as taken from [69] together with electron shell occupation numbers  $n_i$ . The corresponding FWHM contributions to the Doppler broadening of the electron decay signal are separately shown for the dominant contributions coming from Ge source detectors (K, L1-L3, M1-M5, N1-N2) and from the LAr (K, L1-L3, M1-M3). The FWHM value of each atomic shell was derived according to Eq. (A.2)

Shell	$n_i$	$E_{b,i}$ (keV)		FWHM <sub><math>i</math></sub> (keV)	
		Ge	Ar	Ge	Ar
K	2	11.103	3.2059	90.6	47.4
L1	2	1.4146	0.3263	31.7	15.2
L2	2	1.2481	0.2506	29.8	13.3
L3	4	1.217	0.2484	29.5	13.3
M1	2	0.1801	0.0293	11.4	4.6
M2	2	0.1249	0.0159	9.6	3.4
M3	4	0.1208	0.0157	9.4	3.3
M4	4	0.0298	-	4.8	-
M5	6	0.0292	-	4.8	-
N1	2	0.0143	-	3.2	-
N2	2	0.0079	-	2.4	-

Considering both Ge and Ar decays, the Doppler-broadened line shape is given as

$$I(E) \propto N_{e,\text{Ge}} \cdot m_{\text{Ge}} \sum_i^{N_{b,\text{Ge}}} I_{i,\text{det}}(E) \cdot \epsilon_{\text{Ge,det}} + N_{e,\text{Ge}} \cdot m_{\text{Ge}} \sum_i^{N_{b,\text{Ge}}} I_{i,\text{mat}}(E) \cdot \epsilon_{\text{Ge,mat}} + N_{e,\text{Ar}} \cdot m_{\text{Ar}} \sum_i^{N_{b,\text{Ar}}} I_{i,\text{Ar}}(E) \cdot \epsilon_{\text{Ar}}, \quad (\text{A.3})$$

where  $N_{e,\text{Ge}}$  ( $N_{e,\text{Ar}}$ ) is the total number of available electrons in Ge (Ar) atoms,  $m_{\text{Ge}}$  ( $m_{\text{Ar}}$ ) is the total mass of the Ge array (Ar volume), and  $\epsilon_{\text{Ge}}$  ( $\epsilon_{\text{Ar}}$ ) is the detection efficiency in the Ge array of the outgoing photon following an electron decay originating within the Ge (Ar) volume (see Table 2 in Sect. 3). For germanium, sensitive detector contributions (*det*) and contributions from surrounding detector material (*mat*) are taken into account separately.

### B: Empirical background model

The empirical background model, as well as its components (i.e. the  $2\nu\beta\beta$  and the  $^{39}\text{Ar}$  decays), are shown in the top panel of Fig. 10, together with the M1 data (see Sect. 3.1, Fig. 3) to which the model has been fit. A bin width of 1 keV was used, consistent with the analysis procedure presented in this paper. Figure 10 shows

fits in two separate energy regions, i.e. 53 to 207 keV (middle) and 184 to 1033 keV (bottom), together with the corresponding residuals, defined as the difference between expected and observed counts over the square root of the expected counts. The two energy regions visible in the top panel were chosen such that to account for the 25 keV width of the fit window used in DM searches and to correctly handle the change in exposure around 195 keV due to the lowering of trigger thresholds in October 2017.

The empirical modified  $\beta$  distribution modelling the  $^{39}\text{Ar}$   $\beta$  spectrum is based on Eq. (5) of ref. [33], using a  $\beta$  distribution as the baseline distribution. It was restricted to ten free parameters in this use-case: two shape parameters plus shift and scale parameters, for both  $\beta$  components, one modification parameter, and one global amplitude parameter. For the empirical  $2\nu\beta\beta$  distribution, modelled as a tenth-order polynomial vanishing at both 0 keV and the  $Q_{\beta\beta}$  value, five parameters are kept free, analogously to the parametrization presented in [70]. The optimum parameters for both the  $2\nu\beta\beta$  function and the  $^{39}\text{Ar}$  parametrization have been found via a combined histogram fit. Apart from the clear deviations at and around the observed  $\gamma$ -line positions as discussed in Sect. 4.3, the residuals largely fluctuate within the expected 1 and  $2\sigma$  ranges.

The validity of the model was investigated using the reduced  $\chi^2/dof$  estimator where  $dof$  refers to the degrees of freedom. The fit yields  $\chi^2/dof \approx 1.09$  (1.51) for the low (high) energy data set from 53 to 207 (184 to 1033) keV. Including all identified  $\gamma$ -transitions in the high energy range (see Table 3) improves a posteriori the  $\chi^2/dof$  value to 1.06. A further goodness-of-fit measure, the non-parametric Kolmogorov-Smirnov test [71], yields p-values  $p_{KS}$  of 0.99 (0.16) for the low (high) energy data set (0.38 after including a posteriori the identified  $\gamma$ -lines). In summary, no significant deviations between the model and the data were found considering a posteriori all identified  $\gamma$ -transitions. We used the Kolmogorov-Smirnov test also to check the normality of the distribution of the fit residuals. For the fit residuals of the low energy spectrum  $p_{KS}$  equals 0.70. In the high energy range we find  $p_{KS} = 0.005$ , or 0.46 when excluding identified  $\gamma$ -lines. In conclusion, no significant deviation of the distribution of the residuals from normality was observed outside the locations of identified  $\gamma$ -lines.

### C: Statistical frameworks

In this section, the applied statistical methods are described in detail.

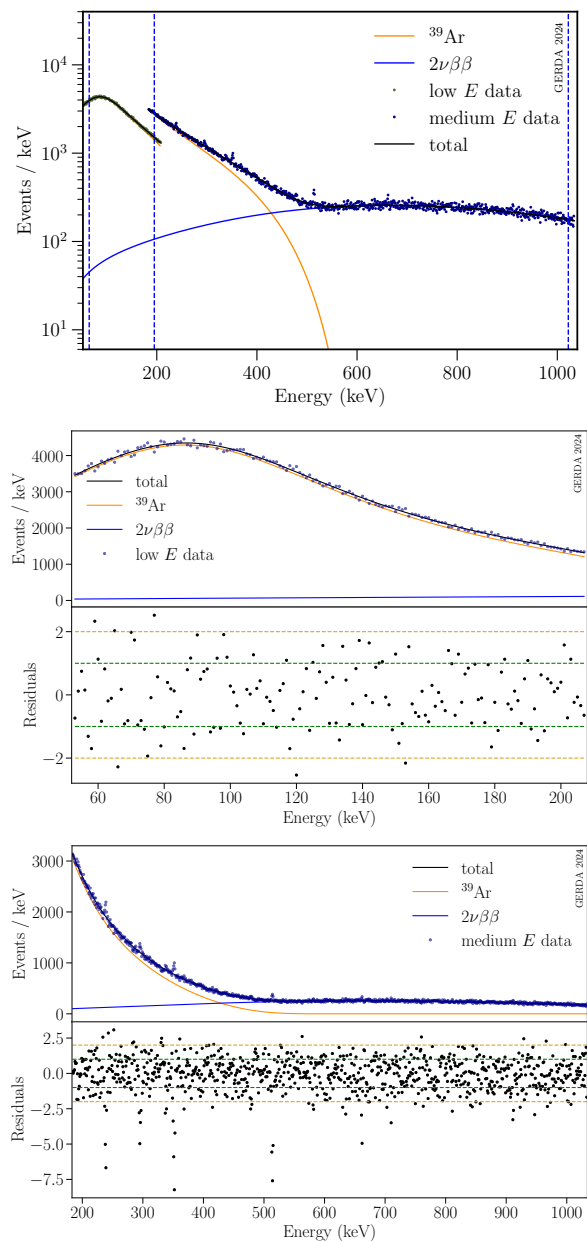


**Fig. 10** Top: empirical background fit model. The fit was performed with a tenth order polynomial and a  $\beta$ -modified  $\beta$  distribution. The vertical dashed, blue lines denote the lowest probed DM mass of 65 keV, the data set transition value of 195 keV, and 1021 keV as the highest potential integer DM mass below  $2m_e$ . Middle, bottom: plots of the data (blue dots) and the model (black line) in the two different energy ranges, i.e. 53-207 keV and 184-1033 keV, with the respective residuals shown below each panel. Residuals are defined as the difference between expected counts and observed counts, normalized by the square root of expected counts

*Bayesian method* To identify a potential excess at any probed energy value, a binned Bayesian fit of the signal peak above the background was performed in the respective signal window. Poisson fluctuations were as-



sumed for bin contents. The Markov-Chain-Monte-Carlo algorithm was applied via the Bayesian Analysis Toolkit (BAT) software [73]. A uniform prior was chosen to constrain the signal amplitude to the physically allowed positive range. The posterior signal distribution was then marginalised via eight Markov chains of  $10^6$  iterations each. The significance of signal strengths having a marginalized posterior distribution incompatible with zero counts was estimated via the global mode divided by the upper and the lower 68% quantiles of the posterior distribution,  $\sigma = \frac{U_{68} - L_{68}}{2}$ . Defining the significance in this manner, the maximally visible excess at 710 keV (see Sect. 4.3), which cannot be attributed to an expected  $\gamma$ -line, has a significance of  $2.9\sigma$ .

*Frequentist method* For the fitting procedure in the Frequentist statistical framework, the local significance was estimated for each of the probed DM candidate masses assuming the asymptotic  $\frac{1}{2}\chi^2(1)$  distribution, cf. [36], where 1 denotes the degrees of freedom. The unexpected excess at 710 keV (see Sect. 4.3) has a local significance of  $3.3\sigma$ . Given the large number of searches, this estimate needs to be corrected for the look-elsewhere effect. The compensation of this effect can be approximated by applying a Bonferroni correction [74], meaning a rescaling of the local p-values by the number of trials. A less conservative option is the method of data-driven self-calibration [75]. The global significance estimation in this method is based on peaks artificially induced into the data. Upon both Bonferroni correction and self-calibration, the observed  $3.3\sigma$  peak corresponds to a global significance  $\leq 1\sigma$ , and might be interpreted as a noise fluctuation. Alternatively, this peak might be of physical origin, i.e. caused by the presence of an unexpected isotope in or near the Ge detectors. The determined limits were obtained with the profile likelihood ratio method [76], partially via the MINUIT2 algorithm [77]. The test statistics  $\tilde{t}$  of [36] was applied to constrain the physical signal strength to positive values, again relying on the asymptotic (non-central)  $\chi^2(1)$  distributions. The median exclusion sensitivity and the non-centrality parameter were estimated from the Asimov data set, as motivated in [36] as well.

#### D: Direct dark matter absorption vs dark Compton scattering

Fig. 11 compares the effect of direct dark matter absorption and dark Compton scattering on the Bayesian limit for the kinetic mixing coupling of DPs to electrons. Including the dark Compton scattering interaction induces a strong sensitivity improvement compared to the

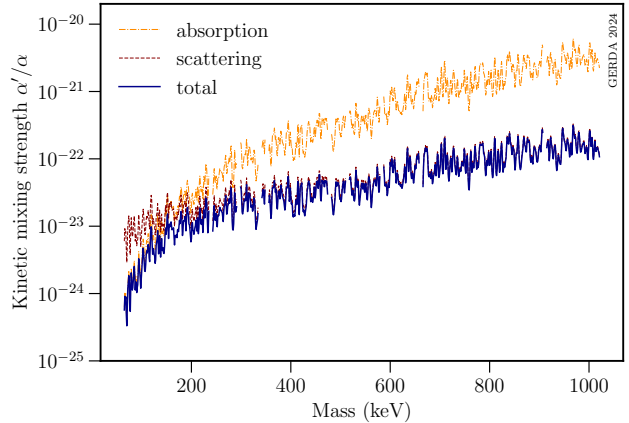


**Fig. 11** Comparison of Bayesian limits at 90% CI for the dimensionless coupling constant of DPs to electrons, plotted as a function of the respective DM mass when evaluated by considering photoelectric-like absorption only (gold), Compton scattering only (red), and both interactions (blue). Regions around identified  $\gamma$  lines (see Sect. 4.3, Table 3) were omitted

previous results [2] at higher energies. The same conclusions hold for the limits on the ALP-electron coupling strengths (not shown). Table 7 shows selected results on the kinetic mixing strength of DPs and the coupling of ALPs to electrons taking both direct dark matter absorption and dark Compton scattering into account.

#### E: Comparison of bosonic dark matter sensitivities

The Bayesian (Frequentist) median sensitivities assuming no signal are plotted for the kinetic mixing coupling of DPs to electrons in Fig. 12, together with the expected 1 and  $2\sigma$  fluctuation bands for the Bayesian limits, as determined from a set of  $10^3$  MC simulations sampled individually at each inspected integer mass value. Here, both the photoelectric-like absorption and Compton scattering processes are taken into account when extracting the coupling values. The Frequentist sensitivities were extracted directly from the Asimov data sets (see Sect. C). The drop visible around 196 keV is related to the difference in exposure between the energy intervals of 65-195 keV (45.5 kg yr) and 196-1021 keV (60.0 kg yr). Upper limits shown in Fig. 11 lie well within the expectation bands. The same behaviour is found for ALP-electron coupling strengths (here not shown).

**Table 7** Bosonic DM upper limits ( $L$ ) and sensitivities ( $S$ ) at 90% CI/CL on the kinetic mixing strength of DPs ( $\alpha'/\alpha$ ) and on the coupling of ALPs to electrons ( $g_{ae}$ ) at indicated masses as determined in the Bayesian and Frequentist frameworks. The photoelectric-like absorption process as well as the dark Compton scattering were included in the DM interaction rate with Ge material when deriving the coupling values. For each mass, the observed best-fit value (*obs.*) is shown together with its significance (*sig.*). For non-positive *obs.* values, the significance is null and not displayed. The extracted upper limits at 90% CI/CL and the median sensitivity for the signal strength are indicated with  $N_{\text{up}}$  and  $N_s$ , respectively. Upper limits derived for all masses between 65 keV and  $2m_e$  are shown in Fig. 7. Sensitivities for the entire mass range are shown in Fig. 12

Mass (keV)	Framework	Signal counts			$\alpha'/\alpha$ (DPs)		$g_{ae}$ (ALPs)	
		<i>obs.</i> ( <i>sig.</i> )	$N_{\text{up}}$	$N_s$	$L$	$S$	$L$	$S$
65	Bayesian	22.2 (0.5 $\sigma$ )	189.7	173.2	$5.7 \times 10^{-25}$	$5.2 \times 10^{-25}$	$2.0 \times 10^{-12}$	$1.9 \times 10^{-12}$
196		23.8 (0.9 $\sigma$ )	171.9	161.4	$1.1 \times 10^{-23}$	$9.9 \times 10^{-24}$	$2.8 \times 10^{-12}$	$2.7 \times 10^{-12}$
1021		0.0	34.4	46.0	$1.1 \times 10^{-22}$	$1.4 \times 10^{-22}$	$3.3 \times 10^{-12}$	$3.8 \times 10^{-12}$
65	Frequentist	-89.4	99.6	177.2	$3.0 \times 10^{-25}$	$5.4 \times 10^{-25}$	$1.5 \times 10^{-12}$	$2.0 \times 10^{-12}$
196		50.5 (0.5 $\sigma$ )	210.9	159.7	$1.3 \times 10^{-23}$	$9.9 \times 10^{-24}$	$3.1 \times 10^{-12}$	$2.7 \times 10^{-12}$
1021		-15.9	31.0	45.8	$1.0 \times 10^{-22}$	$1.4 \times 10^{-22}$	$3.1 \times 10^{-12}$	$3.8 \times 10^{-12}$

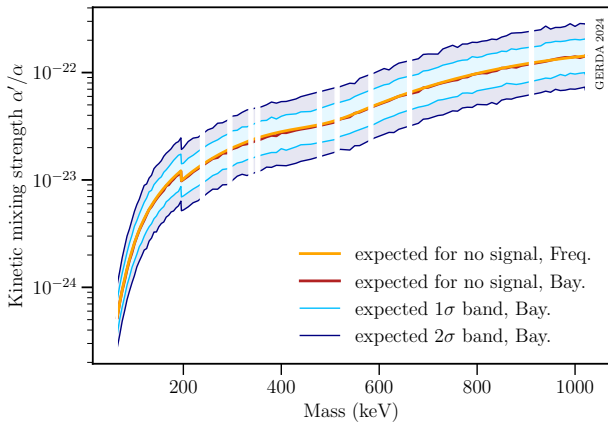


**Fig. 12** Comparison of Bayesian (red) and Frequentist median sensitivities (gold) for the dimensionless coupling constant of DPs, plotted as a function of the respective DM masses. Couplings here are evaluated considering photoelectric-like absorption and Compton scattering processes. The indicated blue bands correspond to the 1 and 2 $\sigma$  range for the Bayesian limits, respectively. Regions around identified  $\gamma$  lines (see Sect. 4.3, Table 3) were omitted

## References

1. M. Pospelov, A. Ritz, M.B. Voloshin, Bosonic super-WIMPs as keV-scale dark matter, *Phys. Rev. D* **78**, 115012 (2008).
2. M. Agostini et al. (GERDA), First Search for Bosonic Superweakly Interacting Massive Particles with Masses up to 1 MeV/ $c^2$  with GERDA, *Phys. Rev. Lett.* **125**, 011801 (2020), [Erratum: *Phys.Rev.Lett.* 129, 089901 (2022)].
3. Y.J. Ko, H. Park, Remarks on bosonic super-WIMP search experiments, *Phys. Rev. D* **104**, 083030 (2021).
4. Y. Hochberg, B. von Krosigk, E. Kuflik, T.C. Yu, Impact of Dark Compton Scattering on Direct Dark Matter Absorption Searches, *Phys. Rev. Lett.* **128**, 191801 (2022).
5. J. Heeck, V. Takhistov, Inclusive nucleon decay searches as a frontier of baryon number violation, *Phys. Rev. D* **101**, 015005 (2020).
6. A.D. Sakharov, Violation of CP Invariance, C asymmetry, and baryon asymmetry of the universe, *Pisma Zh. Eksp. Teor. Fiz.* **5**, 32 (1967).
7. V.A. Mitsou, Dark matter: experimental and observational status, in 15th Marcel Grossmann Meeting on Recent Developments in Theoretical and Experimental General Relativity, Astrophysics, and Relativistic Field Theories (2019).
8. R.K. Ellis et al., Physics Briefing Book: Input for the European Strategy for Particle Physics Update 2020 (2019).
9. R.Z. Ferreira, M.C.D. Marsh, E. Müller, Do Direct Detection Experiments Constrain Axionlike Particles Coupled to Electrons?, *Phys. Rev. Lett.* **128**, 221302 (2022).
10. N. Abgrall et al. (MAJORANA), New limits on Bosonic Dark Matter, Solar Axions, Pauli Exclusion Principle Violation, and Electron Decay from the MAJORANA DEMONSTRATOR, *Phys. Rev. Lett.* **118**, 161801 (2017).
11. I.M. Bloch, R. Essig, K. Tobioka, T. Volansky, T.T. Yu, Searching for Dark Absorption with Direct Detection Experiments, *JHEP* **06**, 087 (2017).
12. Y. Hochberg, T. Lin, K.M. Zurek, Absorption of light dark matter in semiconductors, *Phys. Rev. D* **95**, 023013 (2017).
13. E. Aprile et al. (XENON), Excess electronic recoil events in XENON1T, *Phys. Rev. D* **102**, 072004 (2020).
14. W.J. Huang, M. Wang, F.G. Kondev, G. Audi, S. Naimi, The AME 2020 atomic mass evaluation (I). Evaluation of input data, and adjustment procedures, *Chin. Phys. C* **45**, 030002 (2021).
15. M. Wang, W.J. Huang, F.G. Kondev, G. Audi, S. Naimi, The AME 2020 atomic mass evaluation (II). Tables, graphs and references, *Chin. Phys. C* **45**, 030003 (2021).
16. A. Negret, B. Singh, Nuclear Data Sheets for A = 75, *Nucl. Data Sheets* **114**, 841 (2013).
17. D. Lide, Handbook of Chemistry and Physics, Vol. 85 (2004–2005).
18. H.V. Klapdor-Kleingrothaus, I.V. Krivosheina, I.V. Titkova, A new experimental limit for the stability of the electron, *Phys. Lett. B* **644**, 109 (2007).
19. K.H. Ackermann et al. (GERDA), The GERDA experiment for the search of  $0\nu\beta\beta$  decay in  $^{76}\text{Ge}$ , *Eur. Phys. J. C* **73**, 2330 (2013).
20. M. Agostini et al. (GERDA), Upgrade for Phase II of the GERDA experiment, *Eur. Phys. J. C* **78**, 388 (2018).

21. M. Agostini et al. (GERDA), Final Results of GERDA on the Search for Neutrinoless Double- $\beta$  Decay, *Phys. Rev. Lett.* **125**, 252502 (2020).
22. A. Lubashevskiy et al., Mitigation of  $^{42}\text{Ar}/^{42}\text{K}$  background for the GERDA Phase II experiment, *Eur. Phys. J. C* **78**, 15 (2018).
23. K.T. Knöpfle, B. Schwingenheuer, Design and performance of the GERDA low-background cryostat for operation in water, *JINST* **17**, P02038 (2022).
24. J. Janicskó Csáthy, H. Aghaei Khozani, A. Caldwell, X. Liu, B. Majorovits, Development of an anti-Compton veto for HPGe detectors operated in liquid argon using silicon photo-multipliers, *Nucl. Instr. Methods A* **654**, 225 (2011).
25. K. Freund et al., The Performance of the Muon Veto of the GERDA Experiment, *Eur. Phys. J. C* **76**, 298 (2016).
26. S.Y.F. Chu, L.P. Ekström, R.B. Firestone, WWW Table of Radioactive Isotopes, database version 1999-02-28, accessed 2023-01-23. <http://nucldata.nuclear.lu.se/toi/>
27. XCOM, NIST. <https://www.nist.gov>
28. M. Boswell et al., MaGe-a Geant4-based Monte Carlo Application Framework for Low-background Germanium Experiments, *IEEE Trans. Nucl. Sci.* **58**, 1212 (2011).
29. B. Lehnert, Search for  $2\nu\beta\beta$  Excited State Transitions and HPGe Characterization for Surface Events in GERDA Phase II, Ph.D. thesis, Dresden University of Technology (2016). <https://nbn-resolving.org/urn:nbn:de:bsz:14-qucosa-199454>
30. J.H. Hubbell, S.M. Seltzer, Tables of x-ray mass attenuation coefficients and mass energy-absorption coefficients 1 keV to 20 MeV for elements  $Z = 1$  to 92 and 48 additional substances of dosimetric interest, Tech. Rep. (1995).
31. M. Agostini et al. (GERDA), Calibration of the GERDA experiment, *Eur. Phys. J. C* **81**, 682 (2021).
32. M. Agostini et al. (GERDA), Liquid argon light collection and veto modeling in GERDA Phase II, *Eur. Phys. J. C* **83**, 319 (2023).
33. P. Awodutire, O. Balogun, A. Olapade, E. Nduka, The modified beta transmuted family of distributions with applications using the exponential distribution, *PLoS ONE* **16** (2021).
34. S. Nadarajah, M. Teimouri, S.H. Shih, Modified Beta Distributions, *Sankhya: The Indian Journal of Statistics, B* **76**, 19–48 (2014).
35. M. Agostini et al. (GERDA), Modeling of GERDA Phase II data, *JHEP* **03**, 139 (2020).
36. G. Cowan, K. Cranmer, E. Gross, O. Vitells, Asymptotic formulae for likelihood-based tests of new physics, *Eur. Phys. J. C* **71**, 1554 (2011), [Erratum: *Eur.Phys.J.C* **73**, 2501 (2013)].
37. Wolfram Research, Isotope Data (2014). <https://reference.wolfram.com/language/ref/IsotopeData.html>
38. See Supplemental Material at [URL] for the data shown in Figs. 3, 4 and 7.
39. E. Armengaud et al. (EDELWEISS), Searches for electron interactions induced by new physics in the EDELWEISS-III germanium bolometers, *Phys. Rev. D* **98**, 082004 (2018).
40. I.J. Arnquist et al. (MAJORANA), Exotic Dark Matter Search with the MAJORANA DEMONSTRATOR, *Phys. Rev. Lett.* **132**, 041001 (2024).
41. E. Aprile et al. (XENON), Search for New Physics in Electronic Recoil Data from XENONnT, *Phys. Rev. Lett.* **129**, 161805 (2022).
42. K. Sato (XMASS), Search for dark matter in the form of axion-like particles and hidden photons in the XMASS detector, *J. Phys. Conf. Ser.* **1468**, 012036 (2020).
43. G. Adhikari et al. (COSINE-100), Search for bosonic super-weakly interacting massive particles at COSINE-100, *Phys. Rev. D* **108**, L041301 (2023).
44. C. O'Hare, cajohare/AxionLimits: AxionLimits (2020). <https://cajohare.github.io/AxionLimits/>
45. S.P. Li, X.J. Xu, Production rates of dark photons and  $Z'$  in the Sun and stellar cooling bounds, *JCAP* **09**, 009 (2023).
46. R. Bernabei et al., Search for the nucleon and di-nucleon decay into invisible channels, *Phys. Lett. B* **493**, 12 (2000).
47. R. Bernabei et al., Search for rare processes with DAMA/LXe experiment at Gran Sasso, *Eur. Phys. J. A* **27**, 35 (2006).
48. R. Hazama, H. Ejiri, K. Fushimi, H. Ohsumi, Limits on single- and multinucleon decays in I-127 by inclusive measurements of nuclear gamma and x rays, *Phys. Rev. C* **49**, 2407 (1994).
49. J.C. Evans Jr., R.I. Steinberg, Nucleon Stability: A Geochemical Test Independent of Decay Mode, *Science* **197**, 989 (1977).
50. R.D. Woods, D.S. Saxon, Diffuse Surface Optical Model for Nucleon-Nuclei Scattering, *Phys. Rev.* **95**, 577 (1954).
51. N. Schwierz, I. Wiedenhover, A. Volya, Parameterization of the Woods-Saxon Potential for Shell-Model Calculations (2007). [arXiv:0709.3525](https://arxiv.org/abs/0709.3525) [nucl-th]
52. N. Shimizu, Nuclear shell-model code for massive parallel computation, "KSHHELL" (2013). [arXiv:1310.5431](https://arxiv.org/abs/1310.5431) [nucl-th]
53. A. Volya, Continuum Shell model CoSMo (2016). <https://www.volya.net/index.php?id=cosmo>
54. J. Suhonen, O. Civitarese, Effects of orbital occupancies on the neutrinoless beta beta matrix element of Ge-76, *Phys. Lett. B* **668**, 277 (2008).
55. J.G. Hirsch, P.C. Srivastava, Shell model description of Ge isotopes, *J. Phys. Conf. Ser.* **387**, 012020 (2012)
56. R.L. Workman et al. (Particle Data Group), Review of Particle Physics, *Prog.Theor.Exp.Phys.* 2022 **083C01** (2022 and 2023 update).
57. Y.G. Zdesenko, V.I. Tretyak, To what extent does the latest SNO result guarantee the proton stability?, *Phys. Lett. B* **553**, 135 (2003).
58. T. Araki et al. (KamLAND), Search for the Invisible Decay of Neutrons with KamLAND, *Phys. Rev. Lett.* **96**, 101802 (2006).
59. H.O. Back et al. (Borexino), New limits on nucleon decays into invisible channels with the BOREXINO counting test facility, *Phys. Lett. B* **563**, 23 (2003).
60. A. Allega et al. (SNO+), Improved search for invisible modes of nucleon decay in water with the SNO+ detector, *Phys. Rev. D* **105**, 112012 (2022).
61. A. Derbin, A. Ianni, O. Smirnov, Comment on the statistical analysis in 'A New experimental limit for the stability of the electron' by H.V. Klapdor-Kleingrothaus, I.V. Krivosheina and I.V. Titkova (2007). [arXiv:0704.2047](https://arxiv.org/abs/0704.2047) [hep-ex]
62. M. Agostini et al. (Borexino), Test of the Electric Charge conservation with Borexino, *Phys. Rev. Lett.* **115**, 231802 (2015).
63. I.J. Arnquist et al. (MAJORANA), Search for charge nonconservation and Pauli exclusion principle violation with the MAJORANA DEMONSTRATOR, *Nat. Phys.* (2024), <https://doi.org/10.1038/s41567-024-02437-9>
64. J. Redondo, M. Postma, Massive hidden photons as lukewarm dark matter, *JCAP* **02**, 005 (2009).
65. R.S. Gupta, J. Jaeckel, M. Spannowsky, Probing Poincaré Violation, *JHEP* **11**, 026 (2023).

- 
66. A. Vishneva et al. (Borexino), Test of the electron stability with the Borexino detector, *J. Phys. Conf. Ser.* **888**, 012193 (2017).
  67. N. Abgrall et al. (LEGEND), The Large Enriched Germanium Experiment for Neutrinoless  $\beta\beta$  Decay: LEGEND-1000 Preconceptual Design Report (2021). [arXiv:2107.11462](https://arxiv.org/abs/2107.11462) [physics.ins-det]
  68. P. Agnes et al. (DarkSide), DarkSide-50 532-day Dark Matter Search with Low-Radioactivity Argon, *Phys. Rev. D* **98**, 102006 (2018).
  69. T. Carlson, *Photoelectron and Auger Spectroscopy* (Plenum Press New York, 1975).
  70. H. Primakoff, S.P. Rosen, Double beta decay, *Rept. Prog. Phys.* **22**, 121 (1959).
  71. A.N. Kolmogorov, Sulla Determinazione Empirica di Una Legge di Distribuzione, *Giornale dell'Istituto Italiano degli Attuari* **4**, 83 (1933).
  72. S.S. Shapiro, M.B. Wilk, An analysis of variance test for normality (complete samples), *Biometrika* **52**, 591–611 (December 1965).
  73. A. Caldwell, D. Kollár, K. Kröninger, BAT: The Bayesian Analysis Toolkit, *Comput. Phys. Commun.* **180**, 2197 (2009).
  74. C.E. Bonferroni, *Teoria statistica delle classi e calcolo delle probabilità*, (Seeber, Florence, 1936). <https://books.google.ch/books?id=3CY-HQAACAAJ>
  75. A.E. Bayer, U. Seljak, J. Robnik, Self-calibrating the look-elsewhere effect: fast evaluation of the statistical significance using peak heights, *Mon. Not. Roy. Astron. Soc.* **508**, 1346 (2021).
  76. W.A. Rolke, A.M. López, J. Conrad, Limits and confidence intervals in the presence of nuisance parameters, *Nucl. Instrum. Meth. A* **551**, 493 (2005).
  77. F. James, M. Roos, Minuit: A System for Function Minimization and Analysis of the Parameter Errors and Correlations, *Comput. Phys. Commun.* **10**, 343 (1975).